Incorporating Full Elastodynamic Effects and Dipping Fault Geometries in Community Code Verification Exercises for Simulations of Earthquake Sequences and Aseismic Slip (SEAS)

Brittany A. Erickson[1](bae@uoregon.edu), Junle Jiang[2](jiang@ou.edu),
Valère Lambert[3](valamber@ucsc.edu),
Mohamed Abdelmeguid[4](meguid@illinois.edu)
Martin Almquist[5](martin.almquist@it.uu.se),
Jean-Paul Ampuero[6](ampuero@geoazur.unice.fr),
Ryosuke Ando[7](ando@eps.s.u-tokyo.ac.jp),
Sylvain Barbot[8](sbarbot@usc.edu), Camilla Cattania[9](camcat@mit.edu),
Alexandre Chen[1](chern@cs.uoregon.edu), Luca Dal Zilio[10](dalzilio@caltech.edu),
Eric M. Dunham[12](edunham@stanford.edu),
Ahmed E. Elbanna[4](elbanna2@illinois.edu),
Alice-Agnes Gabriel[13,14](gabriel@geophysik.uni-muenchen.de),
Tobias W. Harvey[1](tharvey2@uoregon.edu), Yihe Huang[15],(yiheh@umich.edu)
Yoshihiro Kaneko[16](kaneko.yoshihiro.4e@kyoto-u.ac.jp),
Jeremy E. Kozdon[17](jkozdon@gmail.com), Nadia Lapusta[11](lapusta@caltech.edu),
Duo Li[13](dli@geophysik.uni-muenchen.de), Meng Li[18](m.li1@uu.nl),
Chao Liang[19](chaovite@gmail.com), Yajing Liu[20](yajing.liu@mcgill.ca),
So Ozawa[7](sozawa@eps.s.u-tokyo.ac.jp),
Casper Pranger[13](casper.pranger@gmail.com),
Paul Segall[12](segall@stanford.edu), Yudong Sun[9](yudong@mit.edu),
Prithvi Thakur[15](prith@umich.edu),
Carsten Uphoff[13](uphoff@geophysik.uni-muenchen.de),
Ylona van Dinther[18](y.vandinther@uu.nl),
Yuyun Yang[12](yyang85@stanford.edu)

[1]University of Oregon, [2]University of Oklahoma,
[3] UC Santa Cruz, [4]University of Illinois Urbana-Champaign, [5]Uppsala University,
[6]Université Côte d'Azur, IRD, CNRS,
Observatoire de la Côte d'Azur, Géoazur, France,
[7]University of Tokyo, [8]University of Southern California,
[9]Massachusetts Institute of Technology, [10]ETH Zurich,
[11]California Institute of Technology,
[12]Stanford University, [13]Ludwig-Maximilians-University,
[14]Scripps Institution of Oceanography, UC San Diego,
[15]University of Michigan, [16]Kyoto University, [17]Naval Postgraduate School,
[18]Utrecht University, [19]Sichuan University, [20]McGill University

Abstract

Numerical modeling of earthquake dynamics and derived insight for seismic hazard relies on credible, reproducible model results. The SEAS (Sequences of Earthquakes and Aseismic Slip) initiative has set out to facilitate community code comparisons, and verify and advance the next generation of physics-based earthquake models that reproduce all phases of the seismic cycle. With the goal of advancing SEAS models to robustly incorporate physical and geometrical complexities, here we present code comparison results from two new benchmark problems: BP1-FD considers full elastodynamic effects and BP3-QD considers dipping fault geometries. Eight modeling groups participated in each benchmark, allowing us to explore these physical ingredients across multiple codes and better understand associated numerical considerations. We find that numerical resolution and computational domain size are critical parameters to obtain matching results, with increasing domain-size requirements posing challenges for volume-based codes even in 2D settings. Codes for BP1-FD implemented different criteria for switching between quasi-static and dynamic solvers, which require tuning to obtain matching results. In BP3-QD, proper remote boundaries conditions consistent with specified rigid body translation are required to obtain matching surface displacements. With these numerical and mathematical issues resolved, we obtain good agreement among codes in long-term fault behavior, earthquake recurrence intervals, and rupture features of peak slip rates and stress drops for both benchmarks. Including full inertial effects generates events with larger slip rates and rupture speeds compared to the quasi-dynamic counterpart. For BP3-QD, both dip angle and sense of motion (thrust versus normal faulting) alter ground motion on the hanging and foot walls, and influence event patterns, with some sequences exhibiting similar-sized characteristic earthquakes, and others exhibiting several earthquakes of differing magnitudes. These findings underscore the importance of considering full dynamics and non-vertical dip angles in SEAS models, as both influence short and long-term earthquake behavior, and associated hazards.

Introduction

Improving our understanding of earthquake processes is essential for minimizing their devastating effects on society and the human environment. Natural fault zones can remain stuck for century- to millennial-long periods until undergoing bursts of rapid sliding during large earthquakes, and it is not well known what governs the recurrence intervals and magnitudes of large events and the associated ground motion. One of the main goals in earthquake science is the development of robust, predictive earthquake models that shed light on what is physically possible and plausible given the inherently limited observations of the Earth. Therefore, an important component of this endeavor is the inclusion of realistic physics and geometries while developing computationally tractable simulations; therefore a spectrum of modeling environments have emerged within the scientific community, with different focuses on the multi-scale features in space and time characterizing earthquake source processes.

At one end of the spectrum of earthquake modeling are the single-event dynamic rupture simulations, which have been extensively used to explore earthquake behavior and rupture propagation. Advanced numerical methods have incorporated a variety of geometric and physical complexities such as non-planar faults and off-fault plasticity, for example *Harris and Day* (1993); *Shi and Day* (2013); *Dunham et al.* (2011). However, single dynamic rupture simulations are generally limited to the time scales of wave propagation (seconds to minutes), and need to grapple with choices in initial conditions, such as proper nucleation procedures under the heterogeneous stress conditions consistent with loading and prior fault slip history over decadal-to-centennial time scales. At the other end of the spectrum are earthquake simulators which were developed to model earthquake sequences on millennial time scales in large-scale, complex fault networks (*Tullis et al.*, 2012a; *Richards-Dinger and Dieterich*, 2012).

To make such large-scale simulations computationally tractable, earthquake simulators rely on simplifying assumptions for fault loading conditions, approximations of seismic wave effects, are limited to the linear elastic bulk material response, and require the use of large computational cells (*Ward*, 2012; *Rundle et al.*, 2006; *Dieterich and Richards-Dinger*, 2010). The missing physical effects, such as aseismic slip, wave-mediated dynamic stress transfers and inelastic bulk response, could potentially dominate earthquake and fault interactions.

A complementary modeling framework to those offered by the dynamic rupture simulations and earthquake simulators are simulations of Sequences of Earthquakes and Aseismic Slip (SEAS) (*Erickson et al.*, 2020; *Jiang et al.*, 2022). SEAS models focus on smaller, regional-scale fault zones and aim to understand what physical factors control the full range of observations of aseismic slip, nucleation locations and the earthquakes themselves (dynamic rupture events), ground shaking, damage zone evolution, afterslip and aftershocks, magnitudes, and recurrence intervals of large earthquakes. Such SEAS models can inform the initial conditions and nucleation procedures for dynamic rupture simulations, as well as provide physics-based approximations for larger-scale and longer-term earthquake simulators.

Earlier methods for SEAS simulations made simplyfing assumptions in order to ease computations, including an assumed linear elastic material response, approximate elastodynamic effects, simple fault geometries (e.g. single planar faults or small fault networks) and/or were limited to two-dimensional (2D) scenarios (e.g. *Tse and Rice*, 1986; *Rice*, 1993). However, recent advancement of SEAS computational methods have enabled simulations with additional physical and/or geometrical features, including full inertial effects, material heterogeneities, and non-planar fault geometries in 3D volumes (e.g., *Lapusta and Rice*, 2003; *Kaneko et al.*, 2011; *Erickson and Dunham*, 2014; *Erickson et al.*, 2017; *Allison and Dunham*, 2018; *Preuss et al.*, 2019; *Dunyu et al.*, 2020; *Romanet and Ozawa*, 2021; *Barbot*, 2021). The inclusion of full inertia (as opposed to the radiation damping approximation of *Rice* (1993)) generates dynamic stress transfers that tend to increase slip rates and rupture speeds (e.g., *Lapusta et al.*, 2000) and can generate qualitatively different event dynamics including pulse-like ruptures (*Thomas et al.*, 2014), the transition to super-shear (e.g., *Andrews*, 1976a; *Harris and Day*, 1993), and the probability that ruptures jump between different fault segments (*Lambert and Lapusta*, 2021). On the other hand, geometric complexities (for example fault non-planarity and non-vertical dipping faults) can significantly alter the resulting ground motion in terms of high-frequency content and asymmetry of shaking across the fault trace which have direct implications for seismic hazard assessment (e.g., *Duan and Oglesby*, 2005; *Ma* *and Beroza*, 2008).

As SEAS models are being used to explain, reproduce, and predict earthquake behavior in more physically and geometrically complex settings, the critical step remains to ensure that these methodologies are accurate. The dynamic rupture simulations and the earthquake simulators have undergone extensive testing, comparing results from different codes developed to address the computational challenges associated with the particular temporal and spatial scales under consideration (*Harris et al.*, 2009; *Barall and Harris*, 2014; *Harris et al.*, 2018; *Tullis et al.*, 2012b). The advancement of SEAS models require similar rigorous testing to verify outcomes over scales specific to SEAS problems: temporal resolution of the pre-, inter-, and post-seismic periods as well as spontaneous earthquake nucleation, and the spatial resolution of physical processes relevant to dynamic wave propagation and longer-term features such as interseismic healing of the fault zone, viscoelasticity, and fluid flow.

Our first two benchmark problems BP1-QD and BP2-QD constitute the very first SEAS code verification exercises (*Erickson et al.*, 2020), where "-QD" means quasi-dynamic approximation. While relatively simple in set-up (e.g. 2D antiplane problem, with a vertically embedded, planar fault), these benchmarks were designed to test the capabilities of different computational methods in correctly solving a mathematically well-defined, basic problem in crustal faulting. Our follow-up benchmark problems addressed important issues in three-dimensional (3D) SEAS simulations, in particular exploring how various numerical and physical factors affect complex observables at often marginal numerical resolutions (*Jiang et al.*, 2022). The success of these exercises have encouraged the SEAS group to consider problems with increased physical and geometric complexities.

In this paper we present results from two new benchmarks, BP1-FD and BP3-QD. Benchmark BP1-FD, with "-FD" indicating a fully dynamic problem, is our first benchmark problem where we consider fully dynamic earthquake rupture and seismic wave propagation, constituting an important step towards incorporating inertial effects into SEAS models. BP3-QD is the first SEAS benchmark considering a 2D plane-strain problem, where a dipping fault intersects the free surface and induces changes in normal stress on the fault. In this work our goal is two-fold: to showcase agreements made across participating codes in the two benchmark problems, and to highlight some of the differences that these added features have on SEAS model outcomes.

We organize the paper as follows: First we provide details of the SEAS working group, including information on participating modeling groups and codes. Then we provide an overview of the SEAS strategy for benchmark design and details the mathematical problem statements for both BP1-FD and BP3-QD. We share results from code comparisons for both benchmarks, along with a discussion of model outcomes influenced by the new physics and geometries considered. The final section provides a summary of findings.

SEAS Coordination and Modeling Groups

The overall goal of the SEAS working group has been to verify SEAS models that address important problems in earthquake science, while maximizing participation within the scientific community. These exercises involve the comparison of different computational methods in order to assess our capacity to accurately resolve detailed fault slip history over a range of time scales. These efforts have required us to better understand the dependence of fault slip history on initial conditions, model spin-up, fault properties, and friction laws.

A total of 8 modeling groups participated in BP1-FD and BP3-QD. Details of the codes and modeling groups are provided in Tables 1-2, along with a summary of computational methods, including spectral boundary element/boundary element (SBEM/BEM), finite difference (FDM), and discontinuous-Galerkin/spectral/finite element (DGFEM/SEM/FEM) methods. SEAS codes also adopt different choices in time-stepping, with the majority of groups using adaptive Runge–Kutta-based methods; further details are available in the references provided. As will be described in the next section, the benchmark problems consider semi-infinite spatial domains. Some numerical schemes must make choices for finite domain sizes and boundary conditions that effectively represent these semi-infinite domains. Details differentiating individual codes and specific choices for these parameters are discussed in later sections when relevant.

Benchmark Descriptions

Here we include specific details of the mathematical problem statements for BP1-FD and BP3-QD, including friction, coordinate system and loading conditions (along with a description of relevant parameters) to aid the analysis and discussion of results.

In both benchmark problems, we assume a planar fault is embedded in a homogeneous, linear elastic half-space defined by

$$(x, y, z) \in (-\infty, \infty) \times (-\infty, \infty) \times (0, \infty),$$

with a free surface at $z = 0$ and z as positive downward, see Figures 1-2. We assume either antiplane shear (BP1-FD) or plane strain motion (BP3-QD), effectively reducing both problems to two dimensions. In the upper section of the fault we equate shear stress τ with fault shear resistance, namely

$$\tau = F(V, \theta, \bar{\sigma}_{\mathrm{n}}), \tag{1}$$

where τ and slip rate V are scalar valued for these 2D problems. We consider rate-and-state friction where $F = \bar{\sigma}_{\mathrm{n}} f(|V|, \theta) \frac{V}{|V|}$, where θ is the state variable (*Dieterich*, 1979; *Ruina*, 1983; *Marone*, 1998). The effective normal stress

$$\bar{\sigma}_{\mathrm{n}} = (\sigma^0 - p^0) + \Delta\sigma \tag{2}$$

takes into account possible changes in normal stress $\Delta\sigma$ induced by slip on the fault, where $\bar{\sigma}_{\mathrm{n}}^0 = (\sigma^0 - p^0)$ is the initial effective normal stress and changes in pore fluid pressure p are neglected. θ evolves according to the aging law (*Ruina*, 1983)

$$\frac{d\theta}{dt} = 1 - \frac{|V|\theta}{L}, \tag{3}$$

where L (denoted D_{c} is previous benchmarks) is the characteristic slip distance. The friction coefficient f is given by a regularized formulation (*Lapusta et al.*, 2000)

$$f(V,\theta) = a \sinh^{-1}\left[\frac{V}{2V_0}\exp\left(\frac{f_0 + b\ln(V_0\theta/L)}{a}\right)\right], \tag{4}$$

where f_0 is a reference friction coefficient for reference slip rate V_0. Depth-dependent frictional parameters a and b define a shallow seismogenic region with velocity-weakening (VW) friction and a deeper velocity-strengthening (VS) region, below which a relative plate motion rate is imposed.

Parameters of important relevance for results in all of our benchmark problems to date include the process zone Λ, which describes the spatial region near the rupture front under which breakdown of fault resistance occurs (*Palmer and Rice*, 1973). For fully dynamic rupture simulations, the size of the process zone decreases with increasing rupture speed and shrinks towards zero as the rupture speed approaches the limiting wave speed (Rayleigh wave speed for plane strain problems and shear wave speed for antiplane problems, e.g *Day et al.*, 2005). For fault models governed by rate- and-state friction, the quasi-static process zone at a rupture speed of 0^+, Λ_0, can be estimated (*Day et al.*, 2005; *Ampuero and Rubin*, 2008; *Perfettini and Ampuero*, 2008) as:

$$\Lambda_0 = C\frac{\mu^* L}{b\,\bar{\sigma}_\mathrm{n}^0}, \tag{5}$$

in which C is a constant of order 1 and μ^* is the effective stiffness of the surrounding material ($\mu^* = \mu$ for antiplane strain and $\mu^* = \mu/(1-\nu)$ for plane strain, where ν is Poisson's ratio).

Another characteristic length scale that has been shown to control model behavior is the critical nucleation size h^*, which governs the minimum extent of the rate-weakening region under which spontaneous nucleation may occur (*Andrews*, 1976b,c; *Rubin and Ampuero*, 2005; *Ampuero and Rubin*, 2008). For 2D problems, the critical nucleation size can be estimated for the aging law (with $0.5 < a/b < 1$) as:

$$h^* = \frac{2}{\pi}\frac{\mu^* bL}{(b-a)^2\bar{\sigma}_\mathrm{n}^0}. \tag{6}$$

Throughout this work we use the term cell size to refer to model resolution, that is, the length between grid points. For numerical methods (such as high-order FEM) that are not based on equally spaced grids, cell size should be interpreted as an average resolution per degree of freedom along the face of an element. In the following sections we provide information on suggested cell size for each benchmark problem that ensures resolution of these length scales.

Computational length scales that have been important in our benchmark problems are those defining the 2D domain: L_x denotes the lateral extent and L_z denotes the depth extent (see Figures 1-2). The problem descriptions consider a semi-infinite half-space, which for many codes means making choices for a representative, finite computational domain size. So while not specified by the problem description, some codes must make choices for L_z and (for volume-based codes) L_x, along with boundary condition type. In our first benchmark comparison, BP1-QD, we found that the domain needed to be sufficiently large before results showed negligible change upon further domain-size increase (at which point results did not depend on boundary condition type). Perhaps unsurprisingly, this domain-size requirement is also true for BP1-FD and BP3-QD. We report choices of numerical parameters that are critical to model agreement across codes, and mainly show and discuss results for simulations with sufficiently large domains sizes.

Complete details of both benchmark problems are included in supplementary material and on our online platform.

BP1-FD Description

BP1-FD is the fully-dynamic version of the first benchmark problem BP1-QD (previously referred to as BP1, see *Erickson et al.* (2020)) and includes the nucleation, propagation (including the generation of seismic waves), and arrest of earthquakes, with aseismic slip in the post- and inter-seismic periods.

For this benchmark problem, the fault is embedded vertically within a semi-infinite half-space and we assume 2D antiplane shear motion governed by the momentum balance equation and Hooke's law of linear elasticity, see Figure 1. The fault intersects the free surface at $z = 0$ and is velocity-weakening down to a depth H, at which point it transitions to velocity strengthening down to a depth W_f. Below W_f the fault creeps at an imposed constant rate V_p down to infinite depth. The fault shear stress $\tau = \tau^0 + \Delta\tau$ involved in Equation (1) is the sum of the prestress and the shear stress perturbation (the effects of radiation damping presented in BP1-QD to bound shear stress at seismic slip rates are naturally incorporated in the fully dynamic stress interactions $\Delta\tau$). We let $u = u(x, z, t)$ denote the out-of-plane displacement, and assume that right-lateral motion corresponds to positive slip values.

As in BP1-QD, the effective normal stress on the fault is equal to the initial effective normal stress ($\bar{\sigma}_\mathrm{n} = \bar{\sigma}_\mathrm{n}^0$), as slip on the fault induces no changes in normal stress. We assume the same parameter values as those in BP1-QD, see *Erickson et al.* (2020), except limit the total simulation time to 1,500 years; all parameters are given here in Table 3 for completeness. A suggested cell size of 25-m ensures that Λ_0 and h^* are resolved with 12 and 80 grid points, respectively.

BP3-QD Description

BP3-QD is our first 2D plane strain problem where a planar fault is embedded in a homogeneous, linear elastic half space, dipping at ψ degrees from horizontal, see Figure 2. The fault intersects the free surface at $z = 0$; the foot wall ($x \leq z \cot\psi$) and the hanging wall ($x \geq z \cot\psi$) are designated by ($-$) and ($+$), respectively. The down-dip distance is denoted x_d. We let $[u, w] = [u(x, z, t), w(x, z, t)]$ denote the vector of in-plane displacements, with u in the (horizontal) x-direction and w in the (vertical) z-direction (with positive values of w downward). We assume a quasi-dynamic response by approximating inertial effects through radiation-damping. Rate-and-state friction acts on the fault interface down to $x_d = W_\mathrm{f}$, where shear stress $\tau = \tau^0 + \Delta\tau - \eta V$ is the sum of the prestress, the shear stress change due to quasi-static deformation, and the radiation damping stress. Similar to BP1-FD, the fault is velocity-weakening down to $x_d = H$, then transitions and is velocity-strengthening down to $x_d = W_\mathrm{f}$. Below W_f, the fault creeps at an imposed constant rate V_p.

For our earlier benchmarks BP1-QD and BP2-QD (and including BP1-FD, considered in this work) we only requested fault station time series, which only involve changes in fields across the fault interface. However, these benchmark problems contain an ambiguity in the assumed boundary conditions at infinity, which was revealed in BP3-QD when considering off-fault stations. We resolved this by specifying that stress changes $\Delta\sigma_{ij}$ and displacement changes (from rigid body translation), $u - u^{\mathrm{rigid}}$ and $w - w^{\mathrm{rigid}}$, vanish at infinity ($x \to \pm\infty, z \to \infty$). The rigid body translation is given by

$$u^{\pm,\mathrm{rigid}}(t) = \mp\frac{V_p t}{2}\cos\psi \tag{7a}$$

$$w^{\pm,\mathrm{rigid}}(t) = \mp\frac{V_p t}{2}\sin\psi, \tag{7b}$$

where both sides of the fault are displaced and reflect the long term, steady-state motion of the fault at depth.

Simulations for BP3-QD are compared for three different dip angles of $\psi = 30^\circ, 60^\circ$ and 90° and for both thrust and normal faulting scenarios. Note that unlike BP1, the non-vertical dipping fault allows for perturbations from the initial effective normal stress $\bar{\sigma}_\mathrm{n}^0$. Our sign conventions are such that thrust faulting has positive values for slip, slip rate and shear traction; normal faulting has negative values. For the vertical fault case these fields will be of equal but opposite values for thrust versus normal faulting, therefore we only share results from the 90° thrust-faulting scenario. For non-vertical faults however, this symmetry is broken by the fault's intersection with the free surface. All parameters are given in Table 4. A suggested cell-size of 25-m resolves Λ_0 and h^* with 16 and 100 grid points, respectively.

Computational Domain Size Considerations

Nearly all of the participating codes in BP1-FD and BP3-QD (Tables 1 and 2) are required to make some choices for finite computational domain lengths that sufficiently capture the response of the half-space. The exceptions to this are the BEM-based codes (Unicycle, FDRA, TriBIE, ESAM and HBI) that only consider the rate-and-state frictional section of the fault, which is discretized down dip to W_f. Below W_f (and down to infinite depth), steady slip at rate V_p is implicitly imposed through backslip loading.

For the spectral boundary-element code (BICyclE) however, the fault is discretized down to a finite depth L_z (below W_f) and subject to periodic boundary conditions, defining a region referred to as a replication cell; in practice the problem includes an infinite number of fault segments of multiples of L_z. L_z must be sufficiently large so that the interaction among the replicated segments is negligible and approaches the infinite fault case with $L_z \to \infty$. Backslip is applied by fixing the slip rate V_p at the edges of the replication cell, which results in the longest wavelength stress interactions being consistent with backslip loading at a fixed plate rate. FEBE, which is a hybrid SBEM/FEM code, also chooses L_z in the same manner as BICyclE.

Pure volume-based codes (GARNET, sem2dpack, Thrase, SPEAR, SCycle, sbplib, FDCycle and tandem) on the other hand, must discretize a 2D domain and determine values for both L_z and L_x that are sufficiently large. While the inclusion of a volume discretization enables the consideration of more complex material properties (e.g. heterogeneities, inelasticity), they are inherently more computationally expensive than those based on BEM, making the exploration of computational domain size an expensive task. To ease computations, all of these volume-based codes (with the exception of SPEAR, which considers a constant cell size throughout the domain) utilize a grid stretching, where high resolution can be localized in a region around the fault. Some codes accomplish this by defining a minimum cell size Δ in the vicinity of the frictional portion of the fault, and gradually coarsening in both directions up to a maximal cell size of $\Delta_{\max}$. Note that cell size is not required to be the same in both the $x-$ and $z-$ directions, but all codes chose to do so. Others use a constant cell size in a region around the fault defined by length scales ℓ_x and ℓ_z (see Figures 1-2). For both benchmark problems we report on choices for domain sizes (that proved sufficiently large) and grid coarsening techniques used.

Comparisons of Simulation Results

In the figures that follow, we showcase comparisons across codes for both BP1-FD and BP3-QD. Labels in the figures provide information on the code used for the simulation results, along with possible exceptions to parameters used (e.g. changes in specified cell size), or information on computational domain size choices.

Except for a few outliers which we note, we obtain good agreements across codes, in the sense that different codes produce similar distributions and values for short-term, co-seismic properties (e.g., peak slip rates, stress drops, rupture speeds and co-seismic surface displacements) as well as long-term features (e.g., number of characteristic events, recurrence times, magnitudes, nucleation locations, off-fault surface displacements), which remain comparable (by visual inspection) throughout the simulation period.

BP1-FD Model Comparisons

BP1-FD constitutes our first benchmark problem that considers fully-dynamic earthquake ruptures over hundreds of years of seismic cycling. To illustrate the differences when including full elastodynamics, Figure 3 presents results from BP1-QD and BP1-FD using the BICyclE code (*Lapusta et al.*, 2000; *Lapusta and Liu*, 2009). In Figure 3(a-b), cumulative slip profiles are plotted in blue contours every year during interseismic loading (when the max slip rate $<$ 1 mm/s) and in red contours every 1 second during coseismic rupture. Figure 3(c) shows calculated recurrence times across all codes, showing good agreements. Also shown are recurrence times from BP1-QD using the BICyclE code. These figures showcase that while both benchmark problems involve characteristic event sequences (after a spin-up period consisting of ∼1-2 events), nucleating at a similar depth of ∼12km, the inclusion of full dynamics shows more slip with each earthquake, corresponding to larger magnitudes and longer recurrence times (∼120 versus 78 years), a marked reflection off the free-surface (missing from the quasi-dynamic simulation), higher slip rates and rupture speeds (evidenced by the vertical and horizontal spacing of red contours, respectively, as discussed in *Thomas et al.* (2014)).

Both BICyclE and FEBE find that a computational domain depth of $L_z = 160$ km is sufficient to capture the response of the half-space. For the volume-based codes, details of the computational parameters are provided in Table 5, including sufficiently large values for L_x and L_z, order of spatial accuracy p, and minimum cell size Δ, used within the vicinity of the fault. Also reported are details of the grid-coarsening techniques that enable good agreements to be made with other codes. While not explored deeply, several volume-based codes (including Thrase and SCycle) found that aggressive grid stretching away from the rate-and-state section of the fault can be detrimental to obtaining good matching results. We attribute this to increased dispersion error from varying cell-size, which can send numerical artifacts back to the fault.

Some codes for BP1-FD naturally handle the seamless transition between quasi-static and fully dynamic treatments of the equations of motion throughout all phases of earthquake sequences (e.g. the BICyclE code of *Lapusta et al.*, 2000). The volume-based code GARNET also seamlessly integrates the elastodynamic equations throughout the entire simulation by utilizing adaptive, implicit time stepping. However, the remaining volume-based codes of this study assume negligible inertial effects during the interseismic phases and integrate the quasi-static equations with explicit, adaptive time-stepping. At the onset of event nucleation, however, inertia is no longer negligible and the elastodynamic equations must be considered. Thus a switching criterion must be implemented, transitioning from the adaptive time-stepping involved in a quasi-static solver, to a small (often constant) time-step, explicit integration technique for the dynamic rupture phase. For example, Thrase switches between solvers based on the maximum slip rate on the fault, whereas SCycle utilizes a switching criterion based on a non-dimensional parameter R (the ratio of the radiation damping term to the quasi-static stress).

Model sensitivity to the switching criterion was left to be explored by individual modeling groups. Table 6 includes information on the strategy used by these volume-based codes, along with the threshold parameter(s) that enabled matching results. For example, Thrase uses the maximum slip rate criterion, switching from a quasi-static to a dynamic solver when $\max(V) > 10$ mm/s and back to quasi-static once $\max(V) < 1$ mm/s. As evidenced in the Table, codes utilizing this $\max(V)$ criterion use non-symmetric threshold parameters, requiring more stringent criteria for switching back to quasi-static. We found in most cases that switching from quasi-static to dynamic was less sensitive to the threshold parameter than switching back; switching too abruptly back to the quasi-static solver can lead to large step changes in shear stress and slip rates, or can lead to frequent switching between solvers due to oscillations in slip rate near the end of a dynamic rupture. Also included in Table 6 are boundary conditions assumed at the finite-domain edges $\pm L_x, L_z$ truncating the half-space, where “QSBC" and “DBC" stand for the boundary condition types assumed in each regime (quasi-static and dynamic, respectively). “disp, free” refers to a displacement condition at $x = \pm L_x$ and a traction free condition at $z = L_z$, whereas “NR" stands for non-reflecting.

Just as for BP1-QD, sufficiently larger domain sizes yield good agreements across codes, as seen in Figure 4 where long-term time series of shear stress and slip rate (at 7.5 km depth) are shown for best model results. Also plotted for comparison are the corresponding time-series for the quasi-dynamic simulations of BP1-QD from the BICyclE code. The fully-dynamic simulations are accompanied with higher shear stresses due to higher slip rates; at this depth the fully dynamic simulations reach a maximum slip rate of $\sim$3 m/s, compared to $\sim$0.5 m/s in the quasi-dynamic simulation. Higher slip rates in the fully dynamic simulations are caused by a much larger wave-mediated dynamic stress concentration and accompanied with a higher stress drop, leading to the increased recurrence times compared with the quasi-dynamic simulation.

We also compared coseismic time series corresponding to the fourth event in BP1-FD, shown in Figure 5. Time (in seconds) is relative to the time at which the slip rate near the nucleation depth ($z = 12.5$ km) first exceeds 10^{-1} m/s. Figure 5(a) shows fault shear stress at $z = 12.5$ km across modeling groups, along with the corresponding time series for the quasi-dynamic simulation BP1-QD. Note that the orange curve of Thrase illustrates the step-change in shear stress that can occur when switching back to the quasi-static solver too abruptly (however in this case the step-change does not significantly alter the long-term agreements with the other model results). Figure 5(b) is the slip rate at $z = 7.5$ km across codes along with those from BP1-QD (also in black). The quasi-dynamic simulation exhibits a lower stress drop and an overall decrease in slip rate at these depths. Showcasing time-series at the two different depths enables an estimate of rupture speed: the quasi-dynamic event propagates more slowly, as illustrated by the later arrival of the surface reflection phase (marked by a black arrow); $\sim$0.4 km/s versus $\sim$1.25 km/s for the fully-dynamic rupture.

BP3-QD Model Comparisons

The 2D plane strain scenario of BP3-QD comes at a higher computational cost than the antiplane shear scenarios of earlier benchmarks BP1-QD and BP2-QD. The suggested cell size of 25-m was not feasible for all participating volume-based codes, and not having a priori knowledge of sufficiently large domain size requirements added to modeling efforts; thus we did not conduct a thorough study on what constitutes a sufficiently large domain. However, in the following paragraphs we share model results and in nearly all cases we obtain good agreements across codes. Some outliers exist that diverge from the others after the first few events, which is not unexpected, as simulation results tend to diverge over time due to round-off error and/or due to differences in domain size choices or other numerical features such as order of accuracy and cell size (*Erickson et al.*, 2020; *Lambert and Lapusta*, 2021). Where qualitative differences exist, we note these outliers and address the discrepancies in the last part of this section.

As in BP1-FD, the volume-based codes discretize a 2D domain and thus also choose values for both L_z and L_x. Table 7 provides an overview of choices made by the volume-based codes including computational domain sizes (L_x and L_z), spatial order of accuracy p, and choice of boundary condition type, where "disp, free" refers to a displacement boundary condition at $x = \pm L_x$ and a traction-free condition at $z = L_z$. Also included in table 7 are details of grid-coarsening techniques implement to ease the computational costs. Although not explored by all the volume-based codes, tandem has found that rather aggressive grid stretching away from the fault may be permissible (*Uphoff et al.*, 2022), which might be due, in part, to the more forgiving nature of quasi-dynamic models that do not suffer the same dispersion errors as fully-dynamic simulations.

We first use BEM-based model results to illustrate the different behaviors between thrust and normal faulting with differing dip angles. Figures 6(a-c) and 7(a-b) show cumulative slip versus distance down dip for each scenario, with blue contours plotted every year during the interseismic period (when the max slip rate < 1 mm/s) and in red every second during coseismic rupture (where negative slip values in the normal faulting case are multiplied by -1 for the sake of comparison). Note that all scenarios involve only surface-rupturing events, all nucleating at or close to 12 km down dip. To better understand these event sequences, in Figures 6(d-e) and 7(c-d) we plot the interevent times across codes. Barring a few outliers (sbplib and TriBIE in 6(e) and sbplib in 6(f)), good agreements are obtained across codes. These figures reveal that the 90° (vertical) case exhibits one characteristic event, nucleating every ∼90 years. For the 60° thrust fault scenario, four characteristic events emerge, with interevent times of ∼60, 87, 90 and 95 years, with longer interevent times corresponding to larger events. The 30° thrust case exhibits two characteristic events with interevent times ∼65 and 80 years. It is interesting to compare these to their normal faulting counterparts, where results across codes exhibit good agreements. For the higher dip angle of 60°, the normal faulting case yields one characteristic event occurring every ∼95 years, which coincides with the interevent time of the largest event in the corresponding thrust faulting scenario, and yet no smaller event types emerge. For the 30° normal faulting case, two characteristic events emerge, similar to its thrust faulting counterpart, but at longer interevent times of ∼75 and 110 years. A better understanding of the influence of fault dip angle and sense of motion on the variability of earthquake sizes is warranted and would require a larger exploration of the parameter space.

Time-series of shear stress and slip rate at the down-dip distance $x_d = 7.5$ km are shown in Figures 8–9 for the three thrust faulting and two normal-faulting scenarios across all participating codes, respectively. In nearly all cases the results show good agreements, barring the few outliers previously mentioned, while also revealing discrepancies not obvious in previous plots: FDCycle in the 60° normal and both FDCycle and sbplib in the 30° normal faulting scenarios. These outliers match each other, and agree qualitatively with the others in the sense that the numbers of characteristic events agree. However there are small but noticeable differences in the interevent times not obvious in Figures 7(c-d). We explore these discrepancies further in the last part of this section.

In Figure 10 we plot the total normal stress at the down-dip distance $x_d = 7.5$ km, associated with each of the non-vertical dipping fault cases (those in which changes in normal stress occur) to better assess overall matching of code results. The overall changes in normal stress at this distance down-dip are only a few percent (our initial effective normal stress was taken to be 50 MPa), however discrepancies in peak values across participating codes are also evident and coincide with the outliers mentioned previously. For the best-matching results however, thrust and normal faulting are accompanied with positive and negative normal stress changes, respectively, with larger changes associated with smaller dip angles.

Next we consider coseismic rupture time-series, plotted in Figures 11-12 across all codes. In Figure 11 we plot shear stress at the down-dip distance $x_d = 12.5$ km for the 4th event in each sequence with time relative to that when the slip rate at this distance down-dip first exceeds 10^{-1}

m/s. Slip rate further up-dip (at $x_d = 7.5$ km depth) is also plotted in Figure 12, which enables an estimate of rupture speed. Barring the outliers noted previously, there is widespread agreement across codes in terms of peak stress and slip rate values and features of the coseismic reflection (noted by a black arrow in the figures). For the thrust fault scenarios, rupture speeds (illustrated by the arrival of the surface reflection phase) do not appear to be significantly affected by dip angle, however maximum slip rates decrease slightly with dip angle, at least at this distance down-dip. For normal faulting, maximum slip rates also decrease with dip angle, and the rupture speed of the 60° simulation appears higher than that of the 30°. To better understand the dependency of rupture characteristics on dip angle warrants further study.

As a final comparison we consider time-series of surface stations across codes, plotted in Figures 13-14. For this benchmark we requested time-series of surface displacements and velocities at distances $x = 0^+, x = \pm 8, \pm 16$ and ± 32 km from the fault trace. Here we only compare surface displacements since some codes do not compute velocities (and some codes do not compute either, hence only a subset of participating codes are plotted here). As mentioned previously, early simulations results revealed major discrepancies across codes brought on by an initial ambiguity in the benchmark problem statement because we did not specify boundary conditions at infinity. After addressing this ambiguity (i.e. adding condition 7), good agreements across codes are obtained. Figure 13 shows the thrust fault results and Figure 14 shows normal fault results, where both horizontal and vertical components of surface displacement at distances $x = 0^+$ km (in thick solid lines) and $x = \pm 16$ km (in thin dashed lines) are shown. We also include (for reference) data for $x = 0^-$ but only from FDCycle (in thin solid lines) as it was not requested in the benchmark description. Stations at distances from the fault trace tend towards the rigid body translation, which we plot (for reference) in yellow and mark with text to indicate motion on the hanging or foot wall.

For the 90° thrust faulting case, shown in Figure 13(a-b), the horizontal components of displacement all fluctuate near or around 0 m (the rigid body motion); positive and negative x values overlap. The vertical displacements are anti-symmetric about $x = 0$, with higher velocities (i.e. larger gradients in displacement per earthquake) at stations closer to the fault trace. For the non-vertical dipping fault cases, both components of displacements reveal asymmetries about $x = 0$.

For both thrust and normal faulting, a dip angle of 60° results in lower total displacements but higher velocities in the horizontal components on the foot wall ($x \leq 0$) at stations near the fault trace, shown in Figures 13(c-d) and 14(a-b), respectively. On the hanging wall, the horizontal surface displacements and velocities approximately track the rigid body translation. Vertical components of velocity however, are higher on the hanging wall ($x \geq 0$) for stations near the fault trace, which experience less total displacement. These features largely align with the findings of *Duan and Oglesby* (2005) for the non-vertical dipping faults, where the horizontal component of ground motion was observed to dominate on the foot wall, while the vertical component dominates on the hanging wall. However, we find that for the 30° dipping fault scenarios (both thrust and normal), shown in Figures 13(e-f) and 14(c-d), the horizontal components of velocity are higher on the hanging wall at stations closer to the fault trace (while the foot wall more closely tracks the rigid body translation).

Reducing Discrepancies in BP3-QD

The computational load of BP3-QD means that exploring numerical dependencies on results (in particular computational domain size) is an expensive task. The volume-based model results shown so far do not match the best BEM results in all cases, which we attribute primarily to the effect of domain size. In Figure 15 we focus on the 60° normal faulting case and compare results from the volume-based code FDcycle to those from BEM-based code FDRA which serves as a reference. Figure 15(a) shows long-term time series of slip rate down dip at $x_d = 12.5$ km for both codes, with FDCycle assuming different values for the computational domain size and numerical parameter choices (with order of accuracy $p = 4$, unless noted otherwise). For small domain sizes (plotted in dark and light blue for different cell sizes), major discrepancies are evident (two characteristic events emerge compared to the single characteristic event sequence in the reference simulation, plotted in black). We increase L_x and L_z two-fold (but maintain a cell size of 200m to support computational feasibility) and these discrepancies are reduced up to a point: the yellow and purple curves show that at least single characteristic events emerge, however the interevent times still differ by several years. Increasing the order of accuracy from $p = 4$ to $p = 6$ (shown in green) does not further reduce the discrepancy either. Figure 15(b) however, shows that this discrepancy can be much further improved by also reducing the grid spacing from 200 m (blue) to 100 m (red). This is further evidenced in the coseismic time series in Figure 15(c) where much improvement is made with smaller grid spacing, but not markedly improved with higher p. The outliers noted in previous sections we posit would benefit from both increased domain size and decreased cell size if computationally feasible.

Summary and Discussion

In this work we find good agreements across participating numerical codes for both benchmark problems. Here we take "good" agreement to mean that many resolved features (over both short and long time scales) appear similar throughout the simulation period. We infer that numerical differences across codes are thus sufficiently small such that the prominent features of these benchmark problems remain comparable (by visual inspection) throughout long-term earthquake sequences, i.e. the numerical differences don't appear to substantially alter the behavior of the system and we therefore believe that the resolved behavior in all the simulations is reliably representative of the physics. A goal for future exercises is to target more quantitative comparisons between simulation results and develop more rigorous metrics to quantify differences between simulated outcomes, such as that of *Day et al.* (2005).

In addition to obtaining agreements, we highlight some of the differences that the added features of full elastodynamics and geometric complexity (dipping faults) have on SEAS model outcomes. BP1-FD enables our first study of numerical considerations for fully dynamic SEAS simulations across a range of codes and computational frameworks. While these simulations need to resolve key physical length scales, computational domain size is a persistent important parameter to obtain matching results. The criteria used by the volume-based codes to switch between methods for the quasi-static and dynamic periods vary across codes and sufficient conditions to obtain matching results is reported. Good agreements across codes are obtained, in terms of number of characteristic events and recurrence times, as well as short term processes (maximum slip rates, stress drops, and rupture speeds). We also compare model response to the quasi-dynamic simulations of BP1-QD. While in both scenarios characteristic events emerge, the simulations of BP1-FD are accompanied by higher slip rates and ruptures speeds, as well as more coseismic slip during dynamic events, and longer interevent times compared to BP1-QD, underscoring the important effects of wave-mediated stress transfers.

For BP3-QD we find good agreements across codes for both thrust and normal faulting and all dip angles considered, except for a few outliers whose discrepancies we attribute to finite computational domain size effects: we demonstrate that we can obtain better matching results of long-term time series by increasing the computational domain size, with some further improvements to short-term, coseismic times series afforded by a decrease in cell size. In terms of model outcomes, the dipping fault geometries and sense of motion (thrust versus normal) yield event sequences ranging from one to four distinct characteristic events (with different interevent times and magnitudes) within a simulation. The comparison of off-fault surface displacements revealed a problem statement ambiguity in the assumed remote boundary conditions, which, once clearly specified, enabled us to obtain good agreements across codes. The simulations reveal notable asymmetry in ground motion on the hanging and foot walls which would have implications for seismic hazard.

BP1-FD and BP3-QD constitute important first steps towards verifying SEAS codes with increased physical and geometric complexities. The ability to explore numerical considerations across a wide variety of codes is invaluable for the advancement of SEAS codes, especially when dependencies on numerical factors (such as the switching criterion used in several volume-based codes for BP1-FD) can be more deeply explored through community efforts, enabling the sharing of successful strategies. In addition, spatial resolution and domain size are computationally costly to explore individually and also benefit from community efforts. However, the associated computational costs will continue to increase with new physical and geometric features, particularly as we move to 3D simulations. Currently, the majority of the volume-based codes involve serial implementations which may inhibit their ability to participate in future benchmarks, unless length scales are chosen carefully to make computations tractable. High-performance computing (HPC) techniques for the volume-based codes will be necessary for future SEAS simulations considering a wider ranges of length scales (requiring higher resolution), and/or 3D simulations.

We expect that future SEAS simulations will regularly include full elastodynamic effects and nonplanar fault geometries, which are known to influence earthquake recurrence times, magnitudes, strong ground shaking and ground motion asymmetry, all of which have important implications for assessment of seismic hazard. We expect to be able to leverage many of the important findings of the Southern California Earthquake Center/U.S. Geological Survey (SCEC/USGS) Spontaneous Rupture Code Verification Project (*Harris et al.*, 2009, 2018; *Barall and Harris*, 2014), not only in advancing SEAS simulations with similar HPC techniques, but also in defining benchmark problems with advanced physical and geometric features (e.g. plasticity, rough faults). An important goal of our SEAS exercises is to also develop insight into appropriate, self-consistent initial conditions prior to rupture that can then inform detailed dynamic rupture simulations. Finally, our future SEAS simulations will aim to consider larger-scale fault systems, including geometrically complex fault networks, and assess the importance of different physical ingredients, such as full inertial effects, for physics-based models of seismic hazard.

Data and Resources: Our online platform (`https://strike.scec.org/cvws/seas/`) is being developed and maintained by Michael Barall. The data for local fault and surface properties are stored on the platform. Supplementary materials include complete descriptions of the two benchmark problems discussed in this work.

Author Contributions: B.A.E. and J.J. designed the benchmark problems and organized the workshops. B.A.E. analyzed results and led the writing of the manuscript with significant input from J.J. and V.L. Remaining authors provided feedback on benchmark design, participated in the benchmark exercises, helped revise the manuscript, and are listed alphabetically.

Acknowledgments: Thanks to Michael Barall who developed and maintains the online platform and to Ruth Harris for mentorship in leading group code verification exercises. B.A.E. and J.J. were supported through the Southern California Earthquake Center, grant no. 18099, 19109, 20113, and 21065. The simulations with BICyclE (J.J.) were conducted with the award EAR170014 from the Extreme Science and Engineering Discovery Environment (XSEDE), which is supported by NSF Grant No. ACI-1548562. The simulations with BICyclE (V.L. and N.L.) were carried out on the High Performance Computing Center cluster of the California Institute of Technology with the grant support from SCEC. J.-P.A. and C.L. were supported by the French National Research Agency through the UCAJEDI Investments in the Future project ANR-15-IDEX-01. T.W.H. was supported by NSF award EAR-1916992 and simulations benefited from access to the University of Oregon high performance computing cluster, Talapas. D.L, C.P, C.U and A.-A.G. were supported by ERC StG TEAR, Grant No. 852992. The simulations with HBI are supported in part by Japan Society for the Promotion of Science (JSPS) KAKENHI Grant No. 19J21676 and 19K04031. M.L, C.P and Y.D were supported by the Dutch Research Council (NWO) grant DEEP.NL.2018.037, Swiss National Science Foundation (SNSF) Grant 200021169880, and EU-MC ITN Grant 604713. A.E.E. and M.A. acknowledge support from NSF CAREER award No. 1753249 and the DOE under Award Number DE-FE0031685. SEAS-themed workshops were funded by SCEC awards no. 17151, 18102, 19110, and 20120. SCEC is funded by NSF Cooperative Agreement EAR-0529922 and USGS Cooperative Agreement 07HQAG0008. This is a SCEC contribution no. xxxx.

References

Abdelmeguid, M., X. Ma, and A. Elbanna, A novel hybrid finite element-spectral boundary integral scheme for modeling earthquake cycles: Application to rate and state faults with low-velocity zones, *Journal of Geophysical Research: Solid Earth*, *124*(12), 12,854–12,881, doi:10.1029/2019jb018036, 2019.

Allison, K., and E. M. Dunham, Earthquake cycle simulations with rate-and-state friction and power-law viscoelasticity, *Tectonophysics*, *733*, 232 – 256, doi:https://doi.org/10.1016/j.tecto.2017.10.021, 2018.

Ampuero, J.-P., and A. M. Rubin, Earthquake nucleation on rate and state faults – Aging and slip laws, *Journal of Geophysical Research: Solid Earth*, *113*(B1), 1–21, doi:10.1029/2007JB005082, 2008.

Andrews, D. J., Rupture velocity of plane strain shear cracks, *Journal of Geophysical Research (1896-1977)*, *81*(32), 5679–5687, 1976a.

Andrews, D. J., Rupture propagation with finite stress in antiplane strain, *J. Geophys. Res.*, *81*, 3575–3582, 1976b.

Andrews, D. J., Rupture velocity of plane strain shear cracks, *J. Geophys. Res.*, *81*, 5679–5687, 1976c.

Barall, M., and R. A. Harris, Metrics for Comparing Dynamic Earthquake Rupture Simulations, *Seismological Research Letters*, *86*(1), 223–235, doi:10.1785/0220140122, 2014.

Barbot, S., Slow-slip, slow earthquakes, period-two cycles, full and partial ruptures, and deterministic chaos in a single asperity fault, *Tectonophysics*, doi:10.1016/j.tecto.2019.228171, 2019.

Barbot, S., A spectral boundary-integral method for quasi-dynamic ruptures of multiple parallel faults, *Bulletin of the Seismological Society of America*, *111*(3), 1614–1630, doi:10.1785/0120210004, 2021.

Bradley, A. M., Software for efficient static dislocation–traction calculations in fault simulators, *Seismological Research Letters*, *85*(6), 1358–1365, doi:10.1785/0220140092, 2014.

Day, S. M., L. A. Dalguer, N. Lapusta, and Y. Liu, Comparison of finite difference and boundary integral solutions to three-dimensional spontaneous rupture, *Journal of Geophysical Research: Solid Earth*, *110*(B12), doi:10.1029/2005JB003813, 2005.

Dieterich, J. H., Modeling of rock friction: 1. experimental results and constitutive equations, *Journal of Geophysical Research: Solid Earth*, *84*(B5), 2161–2168, doi:10.1029/JB084iB05p02161, 1979.

Dieterich, J. H., and K. B. Richards-Dinger, Earthquake recurrence in simulated fault systems, *Pure and Applied Geophysics*, *167*(8), 1087–1104, doi:10.1007/s00024-010-0094-0, 2010.

Duan, B., and D. D. Oglesby, The dynamics of thrust and normal faults over multiple earthquake cycles: Effects of dipping fault geometry, *Bulletin of the Seismological Society of America*, *95*(5), 1623–1636, doi:10.1785/0120040234, 2005.

Dunham, E. M., D. Belanger, L. Cong, and J. E. Kozdon, Earthquake ruptures with strongly rate-weakening friction and off-fault plasticity, part 1: Planar faults, *Bulletin of the Seismological Society*, *101*(5), 2296–2307, doi:10.1785/0120100075, 2011.

Dunyu, L., B. Duan, and B. Luo, EQsimu: a 3-D finite element dynamic earthquake simulator for multicycle dynamics of geometrically complex faults governed by rate- and state-dependent friction, *Geophysical Journal International*, *220*, 598–609, doi:https://doi.org/10.1093/gji/ggz475, 2020.

Erickson, B. A., and E. M. Dunham, An efficient numerical method for earthquake cycles in heterogeneous media: Alternating subbasin and surface-rupturing events on faults crossing a sedimentary basin, *Journal of Geophysical Research: Solid Earth*, *119*(4), 3290–3316, doi:10.1002/2013JB010614, 2014.

Erickson, B. A., E. M. Dunham, and A. Khosravifar, A finite difference method for off-fault plasticity throughout the earthquake cycle, *Journal of Mechanics and Physics of Solids*, *109*, 50 – 77, doi:10.1016/j.jmps.2017.08.002, 2017.

Erickson, B. A., et al., The community code verification exercise for simulating sequences of earthquakes and aseismic slip (seas), *Seismological Research Letters*, *91*, 874–890, doi:10.1785/0220190248, 2020.

Hajarolasvadi, S., and A. E. Elbanna, A new hybrid numerical scheme for modelling elastodynamics in unbounded media with near-source heterogeneities, *Geophysical Journal International*, *211*(2), 851–864, doi:10.1093/gji/ggx337, 2017.

Harris, R. A., and S. M. Day, Dynamics of fault interaction: parallel strike-slip faults, *Journal of Geophysical Research: Solid Earth*, *98*(B3), 4461–4472, doi:10.1029/92JB02272, 1993.

Harris, R. A., et al., The SCEC/USGS dynamic earthquake rupture code verification exercise, *Seismological Research Letters*, *80*, 119–126, doi:10.1785/gssrl.80.1.119, 2009.

Harris, R. A., et al., A suite of exercises for verifying dynamic earthquake rupture codes, *Seismological Research Letters*, *89*(3), 1146–1162, doi:https://doi.org/10.1785/0220170222, 2018.

Jiang, J., et al., Community-driven code comparisons for three-dimensional dynamic modeling of sequences of earthquakes and aseismic slip, *Journal of Geophysical Research: Solid Earth*, *127*(3), e2021JB023,519, doi:https://doi.org/10.1029/2021JB023519, 2022.

Kaneko, Y., J.-P. Ampuero, and N. Lapusta, Spectral-element simulations of long-term fault slip: Effect of low-rigidity layers on earthquake-cycle dynamics, *J. Geophys. Res.-Sol. Ea.*, *116*(B10), 1–18, doi:10.1029/2011JB008395, 2011.

Kozdon, J., B. A. Erickson, and L. C. Wilcox, Hybridized summation-by-parts finite difference methods, *Journal of Scientific Computing*, *87*(85), 1–28, doi:10.1007/s10915-021-01448-5, 2020.

Kozdon, J. E., B. A. Erickson, , and T. Harvey, Preprint: A non-stiff summation-by-parts finite difference method for the wave equation in second order form: Characteristic boundary conditions and nonlinear interfaces, doi:2106.00706, 2021.

Lambert, V., and N. Lapusta, Resolving simulated sequences of earthquakes and fault interactions: Implications for physics-based seismic hazard assessment, *Journal of Geophysical Research: Solid Earth*, *126*(10), e2021JB022,193, doi:https://doi.org/10.1029/2021JB022193, 2021.

Lapusta, N., and Y. Liu, Three-dimensional boundary integral modeling of spontaneous earthquake sequences and aseismic slip, *Journal of Geophysical Research: Solid Earth*, *114*(B9), 1–25, doi:10.1029/2008JB005934, 2009.

Lapusta, N., and J. R. Rice, Nucleation and early seismic propagation of small and large events in a crustal earthquake model, *Journal of Geophysical Research*, *108*(B4, 2205), 1–18, 2003.

Lapusta, N., J. R. Rice, Y. Ben-Zion, and G. Zheng, Elastodynamic analysis for slow tectonic loading with spontaneous rupture episodes on faults with rate- and state-dependent friction, *Journal of Geophysical Research: Solid Earth*, *105*(B10), 23,765–23,789, doi:10.1029/2000JB900250, 2000.

Li, D., and Y. Liu, Spatiotemporal evolution of slow slip events in a nonplanar fault model for northern cascadia subduction zone, *Journal of Geophysical Research: Solid Earth*, *121*(9), 6828–6845, doi:10.1002/2016jb012857, 2016.

Li, D., and Y. Liu, Modeling slow-slip segmentation in cascadia subduction zone constrained by tremor locations and gravity anomalies, *Journal of Geophysical Research: Solid Earth*, *122*, 3138–3157, doi:10.1002/2016JB013778, 2017.

Li, M., C. Pranger, and Y. van Dinther, Characteristics of earthquake cycles: a cross-dimensional comparison of 1d to 3d simulations, *Earth and Space Science Open Archive*, p. 50, doi:10.1002/essoar.10509020.2, 2021.

Liu, Y., and J. R. Rice, Spontaneous and triggered aseismic deformation transients in a subduction fault model, *Journal of Geophysical Research: Solid Earth*, *112*(B09404), 1–23, doi:10.1029/2007JB004930, 2007.

Ma, S., and G. Beroza, Rupture dynamics on a bimaterial interface for dipping faults, *Bulletin of The Seismological Society of America*, *98*, 1642–1658, doi:10.1785/0120070201, 2008.

Marone, C., Laboratory-derived friction laws and their application to seismic faulting, *Ann. Rev. Earth Pl. Sc.*, *26*(1), 643–696, doi:10.1146/annurev.earth.26.1.643, 1998.

Ozawa, S., and R. Ando, Mainshock and aftershock sequence simulation in geometrically complex fault zones, *Journal of Geophysical Research: Solid Earth*, *126*(2), e2020JB020,865, doi:https://doi.org/10.1029/2020JB020865, 2021.

Palmer, A. C., and J. R. Rice, The growth of slip surfaces in the progressive failure of over-consolidated clay, *Proceedings of the Royal Society A*, *332*(1591), 527–548, doi:10.1098/rspa.1973.0040, 1973.

Perfettini, H., and J.-P. Ampuero, Dynamics of a velocity strengthening fault region: Implications for slow earthquakes and postseismic slip, *Journal of Geophysical Research: Solid Earth*, *113*(B9), 1–22, doi:10.1029/2007JB005398, 2008.

Pranger, C., Unstable physical processes operating on self-governing fault systems, improved modeling methodology, Ph.D. thesis, ETH Zurich, 2020.

Preuss, S., R. Herrendörfer, T. Gerya, J.-P. Ampuero, and Y. van Dinther, Seismic and aseismic fault growth lead to different fault orientations, *Journal of Geophysical Research: Solid Earth*, *124*(8), 8867–8889, 2019.

Rice, J. R., Spatio-temporal complexity of slip on a fault, *Journal of Geophysical Research*, *98*(B6), 9885–9907, 1993.

Richards-Dinger, K., and J. H. Dieterich, RSQSim earthquake simulator, *Bulletin of the Seismological Society of America.*, *83*(6), 983–990, doi:10.1785/0220120105, 2012.

Romanet, P., and S. Ozawa, Fully Dynamic Earthquake Cycle Simulations on a Nonplanar Fault Using the Spectral Boundary Integral Element Method (sBIEM), *Bulletin of the Seismological Society of America*, *112*(1), 78–97, doi:10.1785/0120210178, 2021.

Rubin, A. M., and J.-P. Ampuero, Earthquake nucleation on (aging) rate and state faults, *Journal of Geophysical Research: Solid Earth*, *110*(B11), 1–24, doi:10.1029/2005JB003686, 2005.

Ruina, A., Slip instability and state variable friction laws, *Journal of Geophysical Research: Solid Earth*, *88*(B12), 10,359–10,370, doi:10.1029/JB088iB12p10359, 1983.

Rundle, P. B., J. Rundle, K. Tiampo, A. Donnellan, and D. Turcotte, Virtual California: Fault model, frictional parameters, applications, in *Computational Earthquake Physics: Simulations, Analysis and Infrastructure, Part I*, edited by X.-c. Yin, P. Mora, A. Donnellan, and M. Matsu'ura, pp. 1819–1846, Birkhäuser Basel, Basel, 2006.

Segall, P., and A. M. Bradley, Slow-slip evolves into megathrust earthquakes in 2D numerical simulations, *Geophysical Research Letters*, *39*(18), 1–5, doi:10.1029/2012GL052811, 2012.

Shi, Z., and S. M. Day, Rupture dynamics and ground motion from 3-D rough-fault simulations, *Journal of Geophysical Research: Solid Earth*, *118*, 1–20, doi:10.1002/jgrb.50094, 2013.

Thomas, M. Y., N. Lapusta, H. Noda, and J.-P. Avouac, Quasi-dynamic versus fully dynamic simulations of earthquakes and aseismic slip with and without enhanced coseismic weakening, *Journal of Geophysical Research: Solid Earth*, *119*, 1986–2004, 2014.

Tse, S. T., and J. R. Rice, Crustal earthquake instability in relation to the depth variation of frictional slip properties, *J. Geophys. Res.*, *91*(B9), 9452–9472, 1986.

Tullis, T. E., et al., Generic earthquake simulator, *Seismological Research Letters.*, *83*, 959–963, doi:10.1785/0220120093, 2012a.

Tullis, T. E., et al., Comparison among observations and earthquake simulator results for the allcal2 California fault model, *Seismol. Res. Lett.*, *83*, 994–1006, 2012b.

Uphoff, C., M. D. A., and A.-A. Gabriel, Preprint: A discontinuous Galerkin method for sequences of earthquakes and aseismic slip on multiple faults using unstructured curvilinear grids, doi: https://doi.org/10.31223/X50627, 2022.

Ward, S. N., ALLCAL Earthquake Simulator, *Seismological Research Letters*, *83*(6), 964–972, doi: 10.1785/0220120056, 2012.

Table 1: BP1-FD: Details of participating SEAS codes and modeling groups.

Code Name	**Type**	**`Simulation`**[†] (Group Members)	**References**
FEBE	Hybrid FEM/SBEM	`abdelmeguid` (Abdelmeguid, Elbanna)	*Hajarolasvadi and Elbanna* (2017) *Abdelmeguid et al.* (2019)
GARNET	FDM	`li` (M. Li, Dal Zilio, Pranger, van Dinther)	*Pranger* (2020); *Li et al.* (2021) https://bitbucket.org/cpranger/garnet/
sem2dpack	SEM	`liang` (Liang, Ampuero)	`https://github.com/jpampuero/sem2dpack`
Thrase	FDM	`harvey` (Harvey, Chen, Kozdon, Erickson)	*Kozdon et al.* (2020, 2021) `https://github.com/Thrase/Thrase`
BICyclE	SBEM	`jiang` (Jiang) `lambert` (Lambert, Lapusta)	*Lapusta et al.* (2000); *Lapusta and Liu* (2009)
SPEAR	SEM	`thakur` (Thakur, Huang, Kaneko)	`https://github.com/thehalfspace/Spear`
SCycle	FDM	`yang` (Yang, Dunham)	`https://github.com/kali-allison/SCycle`

[†] The names of simulations displayed on our online platform

Table 2: BP3-QD: Details of participating SEAS codes and modeling groups.

Code Name	**Type**	Simulation† (Group Members)	**References**
sbplib	FDM	almquist (Almquist, Dunham)	https://doi.org/10.1016/j.jcp.2020.109842 https://sourceforge.net/projects/elastic-package-test/
Unicycle	BEM	barbot (Barbot)	*Barbot* (2019) https://bitbucket.org/sbarbot
FDRA	BEM	cattania (Cattania, Sun, Segall)	*Segall and Bradley* (2012); *Bradley* (2014)
TriBIE	BEM	dli (D. Li, Gabriel)	*Li and Liu* (2016, 2017)
FDCycle	FDM	erickson (Erickson)	*Erickson and Dunham* (2014) https://github.com/brittany-erickson/FDCycle
ESAM	BEM	liu (Y. Liu)	*Liu and Rice* (2007)
HBI	BEM	ozawa (Ozawa, Ando)	*Ozawa and Ando* (2021) https://github.com/sozawa94/hbi
tandem	DGFEM	uphoff (Uphoff, Gabriel)	https://github.com/TEAR-ERC/tandem

† The names of simulations displayed on our online platform

Table 3: Parameter values used in BP1-FD.

Parameter	Definition	Value, Units
ρ	density	2670 kg/m^3
c_{s}	shear wave speed	3.464 km/s
σ_{n}	effective normal stress on fault	50 MPa
a_0	rate-and-state direct effect parameter	0.010
$a_{\max}$	rate-and-state direct effect parameter	0.025
b_0	rate-and-state evolution effect parameter	0.015
L	characteristic slip distance	0.008 m
V_{p}	plate rate	10^{-9} m/s
V_{init}	initial slip rate	10^{-9} m/s
V_0	reference slip rate	10^{-6} m/s
f_0	reference friction coefficient	0.6
H	depth extent of uniform VW region	15 km
h	width of VW-VS transition zone	3 km
W_{f}	width of rate-and-state fault	40 km
Δz	suggested cell size	25 m
t_{f}	final simulation time	1500 years
L_z	depth of computational domain	not specified
L_x	off-fault distance of computational domain	not specified

Table 4: Parameter values used in BP3-QD. Plus/minus signs refer to thrust/normal faulting, respectively.

Parameter	Definition	Value, Units
ψ	dip angle	$30°$, $60°$, and $90°$
ρ	density	2670 kg/m^3
ν	Poisson's ratio	0.25
c_s	shear wave speed	3.464 km/s
$\bar{\sigma}_\mathrm{n}^0$	initial effective normal stress on fault	50 MPa
a_0	rate-and-state direct effect parameter	0.010
a_max	rate-and-state direct effect parameter	0.025
b_0	rate-and-state evolution effect parameter	0.015
L	characteristic slip distance	0.008 m
V_p	plate rate	$\pm 10^{-9}$ m/s
V_L	prescribed fault slip rate at depth	$\pm 10^{-9}$ m/s
V_init	initial slip rate	$\pm 10^{-9}$ m/s
V_0	reference slip rate	10^{-6} m/s
f_0	reference friction coefficient	0.6
H	down-dip extent of uniform VW region	15 km
h	width of VW-VS transition zone	3 km
W_f	width of rate-and-state fault	40 km
Δz	suggested cell size	25 m
t_f	final simulation time	1500 years
L_z	depth of computational domain	not specified
L_x	off-fault distance of computational domain	not specified

Table 5: Computational parameter values used in volume-based codes for BP1-FD, unless otherwise noted (see text for more details).

Code	L_x, L_z	p	Δ	grid-coarsening
FEBE	n/a, 160 km	2	25 m	n/a
GARNET	$160, 80$ km	8	25 m	$\Delta_{\max} = 200$ m
sem2dpack	$160, 160$ km	4	25 m	$\Delta_{\max} = 500$ m
Thrase	$160, 160$ km	4	50 m	$\ell_x, \ell_z = 125, 125$ km
SPEAR	$160, 160$ km	5	50 m	n/a
SCycle	$160, 160$ km	4	25 m	$\ell_x, \ell_z = 40, 40$ km

Table 6: Details of the different boundary conditions assumed and the switching criterion used by a subset of volume-based codes for BP1-FD (see text for more details).

Code	QSBC	DBC	Switching (type, parameters)
FEBE	n/a, free	NR	$R = 10^{-4}$
sem2dpack	disp, free	NR	$\max(V)$, 3 mm/s, 2 mm/s
Thrase	disp, free	NR	$\max(V)$, 10 mm/s, 1 mm/s
SPEAR	disp, free	NR	$\max(V)$, 5 mm/s, 2 mm/s
SCycle	disp, free	NR	$R = 10^{-4}$

Table 7: Computational parameter values used in volume-based codes for BP3-QD, unless otherwise noted (see text for more details).

Code	L_x, L_z	p	Δ	grid-coarsening	BC
sbplib	$150, 100$ km	6	100 m	$\ell_x, \ell_d = 5, 45$ km	disp, free
FDCycle	$400, 400$ km ($\psi = 90°$)	4	100 m (thrust)	$\ell_x, \ell_d = 40, 40$ km	disp, free
	$200, 200$ km ($\psi = 30°$)		200 m (normal)		
	$100, 100$ km ($\psi = 60°$)				
tandem	$3400, 3400$ km	8	31.25 m	$\Delta_{\max} = 12.5$ km	disp, free

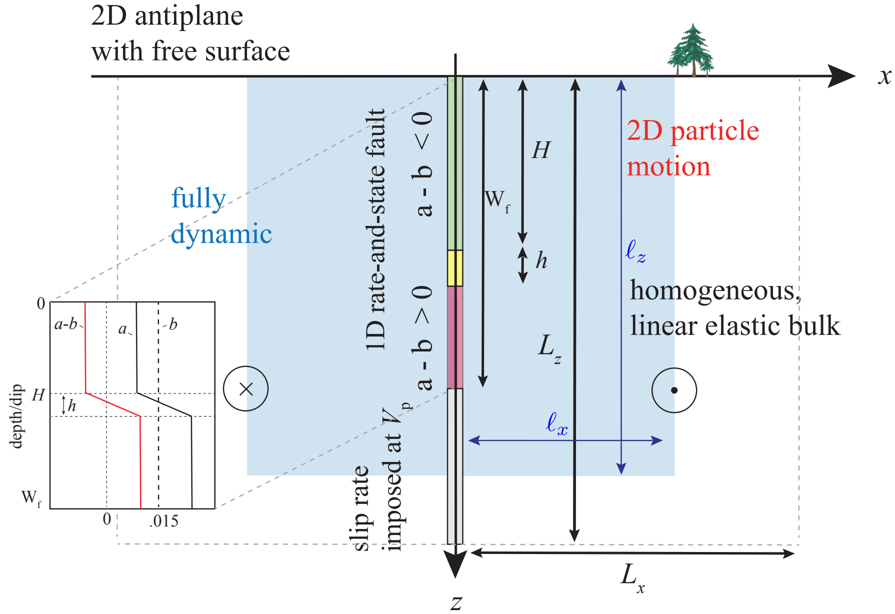

Figure 1: BP1-FD considers a planar fault embedded in a homogeneous, linear elastic half-space with a free surface where motion is antiplane shear. The fault is governed by rate-and-state friction down to the depth $W_{\rm f}$ and creeps at an imposed constant rate $V_{\rm p}$ down to the infinite depth. The fully-dynamic simulations include the nucleation, propagation, and arrest of earthquakes, and aseismic slip in the post- and inter-seismic periods.

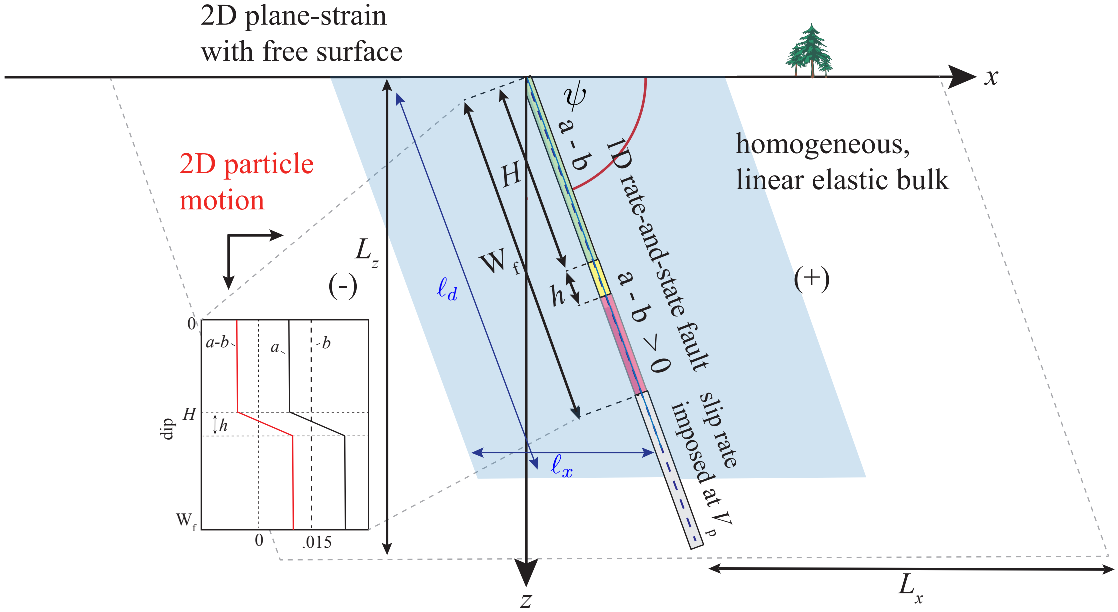

Figure 2: BP3-QD considers a planar, dipping fault embedded in a homogeneous, linear elastic half-space with a free surface where motion is plane strain. The fault is governed by rate-and-state friction down dip to a distance W_f and creeps at an imposed constant rate V_p down to the infinite dip distance. The quasi-dynamic simulations will include the nucleation, propagation, and arrest of earthquakes, and aseismic slip in the post- and inter-seismic periods. The left and right sides of the fault are labeled with “(-)" and “(+)", respectively.

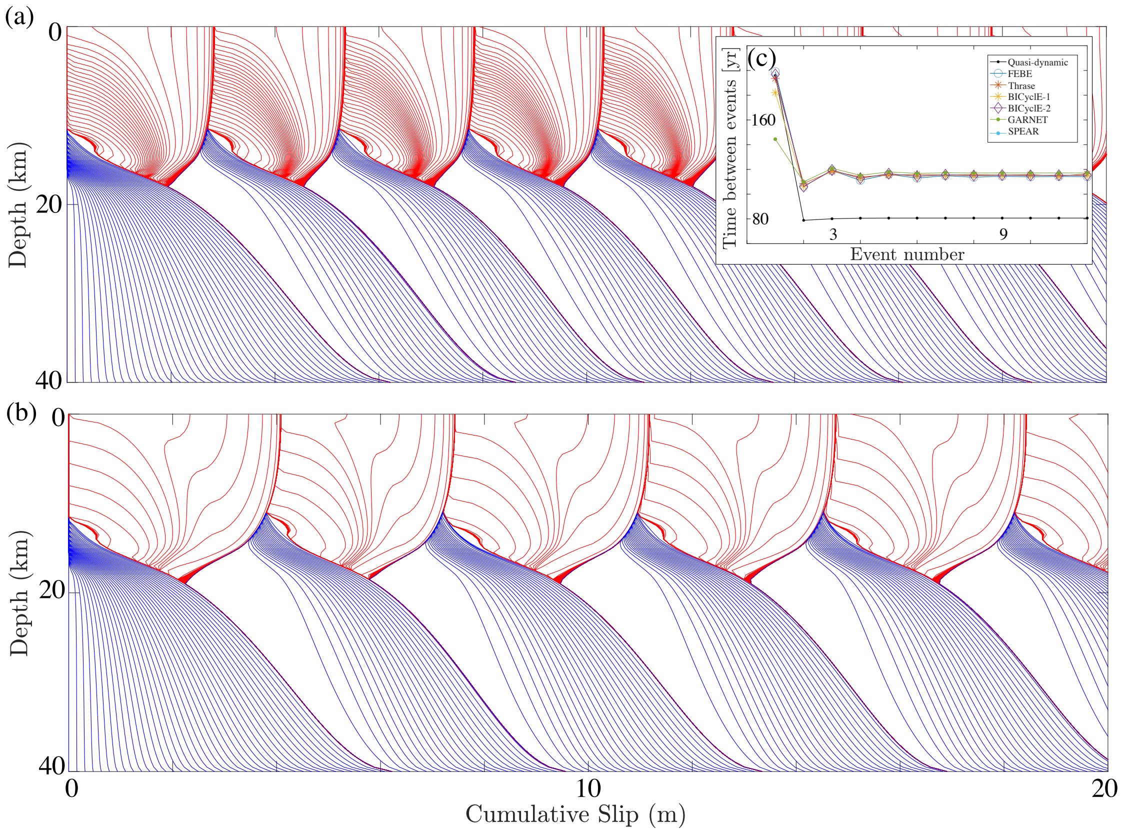

Figure 3: Cumulative slip profiles for (a) BP1-QD and (b) BP1-FD plotted in blue contours every 5 years during the interseismic phases and in red every second during coseismic rupture. BP1-QD results taken from the BICyclE code, with $L_z = 160$ km. After a spin-up period of approximately two events, characteristic event sequences emerge for both BP1-FD and BP1-QD. (c) Recurrence times for BP1-FD (∼120 years) across all codes and for BP1-QD (∼78 years).

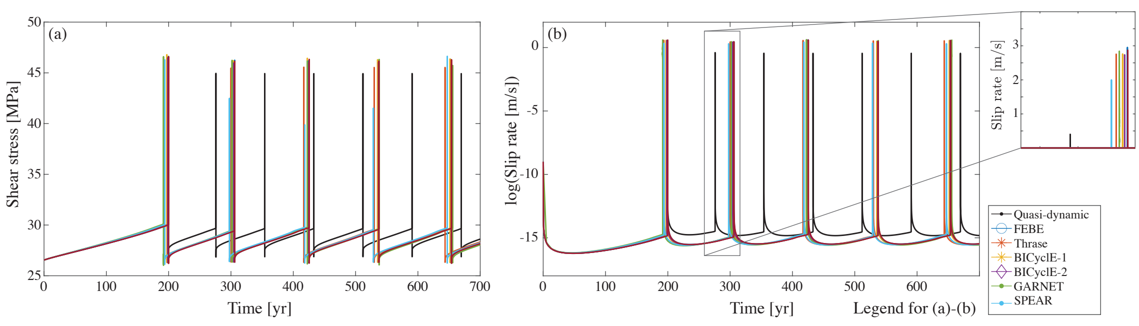

Figure 4: Long-term behavior of BP1-FD models. (a) Shear stress and (b) slip rates at the depth of 7.5 km across codes with sufficiently large computational domain sizes. Also shown (in black) are those for the quasi-dynamic counterpart BP1-QD.

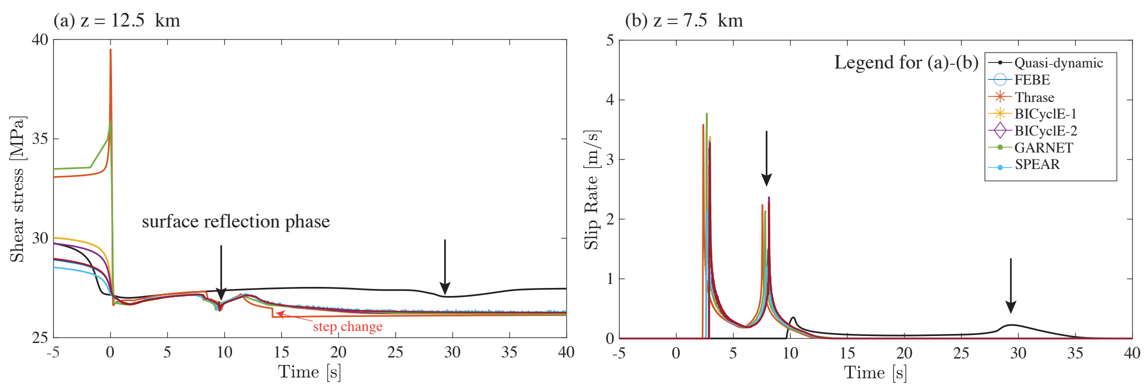

Figure 5: Coseismic behavior of BP1-FD across codes with sufficiently large computational domain sizes during the 8th event, shown for (a) shear stresses at 12.5 km depth and (b) slip rates at 7.5 km depth. Also shown (in black) are those for the quasi-dynamic counterpart BP1-QD. Time (in seconds) is relative to the time at which the slip rate near the nucleation depth (z = 12.5 km) first exceeds 10^{-1} m/s; the 8th QD event occurs a few hundred years before the 8th FD event. The surface reflection phase is marked by a black arrow. The orange arrow in (a) illustrates how a step change in shear stress can occur (in this case for the Thrase code) when switching abruptly back to a quasi-static solver.

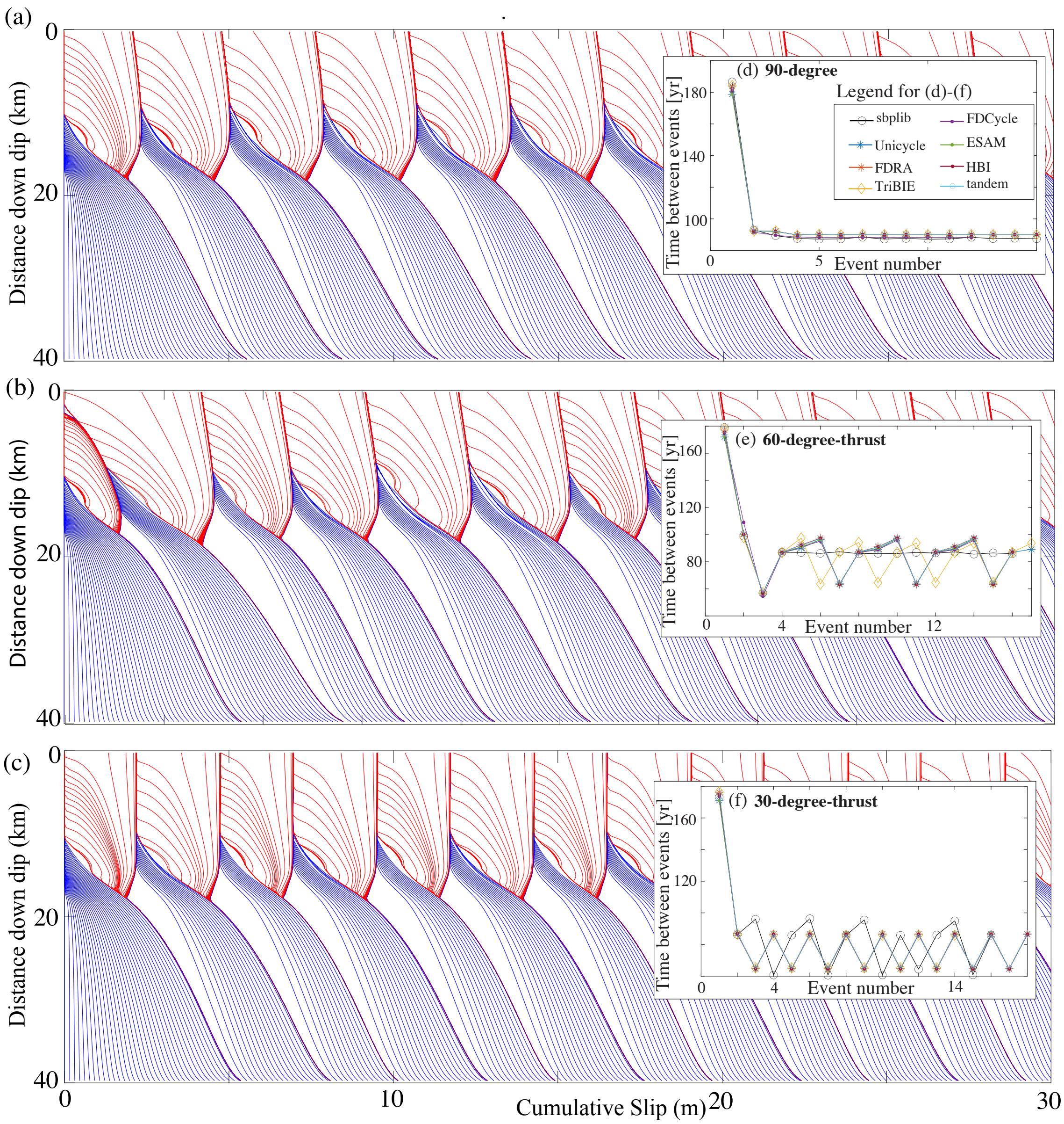

Figure 6: Cumulative slip profiles for BP3-QD thrust-faulting simulations from the FDRA code with dip angles (a) 90° (b) 60° and (c) 30° plotted in blue contours every 5 years during the interseismic phases and in red every second during coseismic rupture. Interevent times for corresponding simulations across all participating codes shown in (d) for 90°, where characteristic events emerge every ∼90 years; (e) for 60°, where four distinct event types emerge every ∼60, 87, 90 and 95 years; (f) for 30°, where two characteristic events emerge every ∼65 and 80 years.

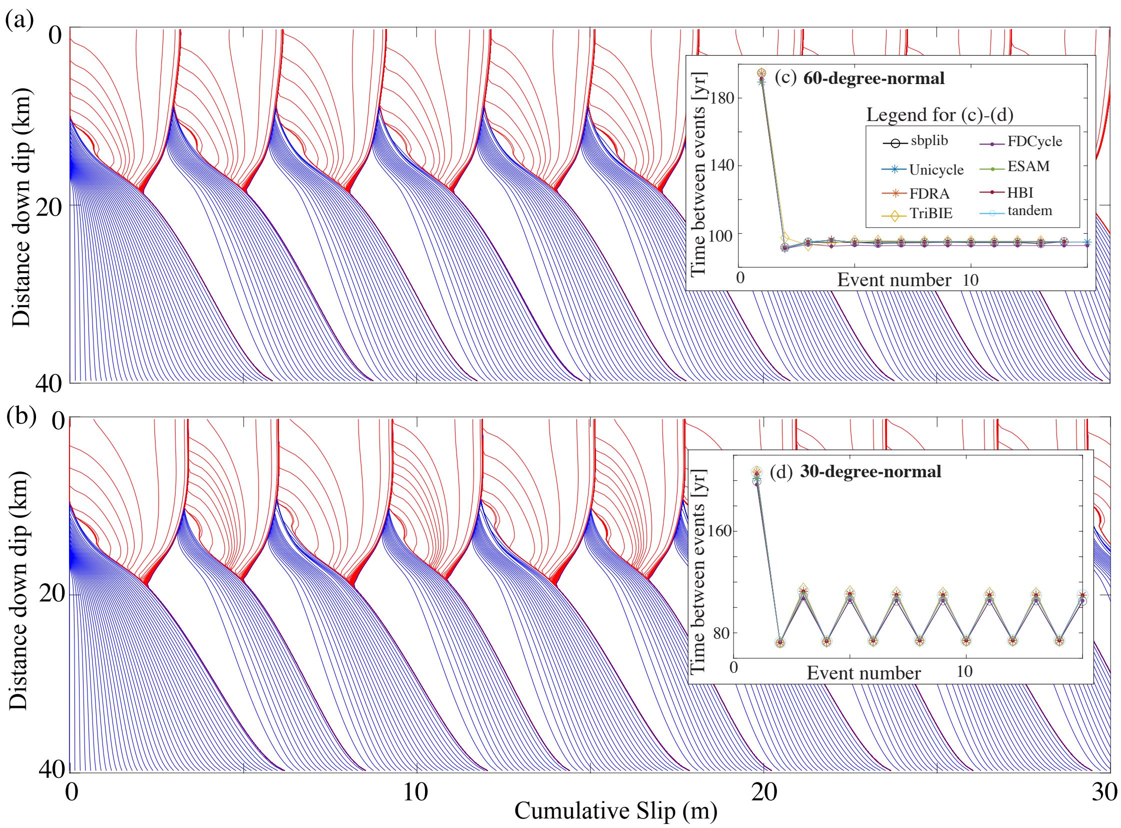

Figure 7: Cumulative slip profiles for BP3-QD normal-faulting simulations from the FDRA code (with slip multiplied by -1) with dip angles (a) 60° and (b) 30° plotted in blue contours every 5 years during the interseismic phases and in red every second during coseismic rupture. Interevent times for corresponding simulations across all participating codes shown in (c) for 60°, where characteristic events emerge every ∼95 years; (d) for 30°, where two distinct event types emerge every ∼75 and 110 years.

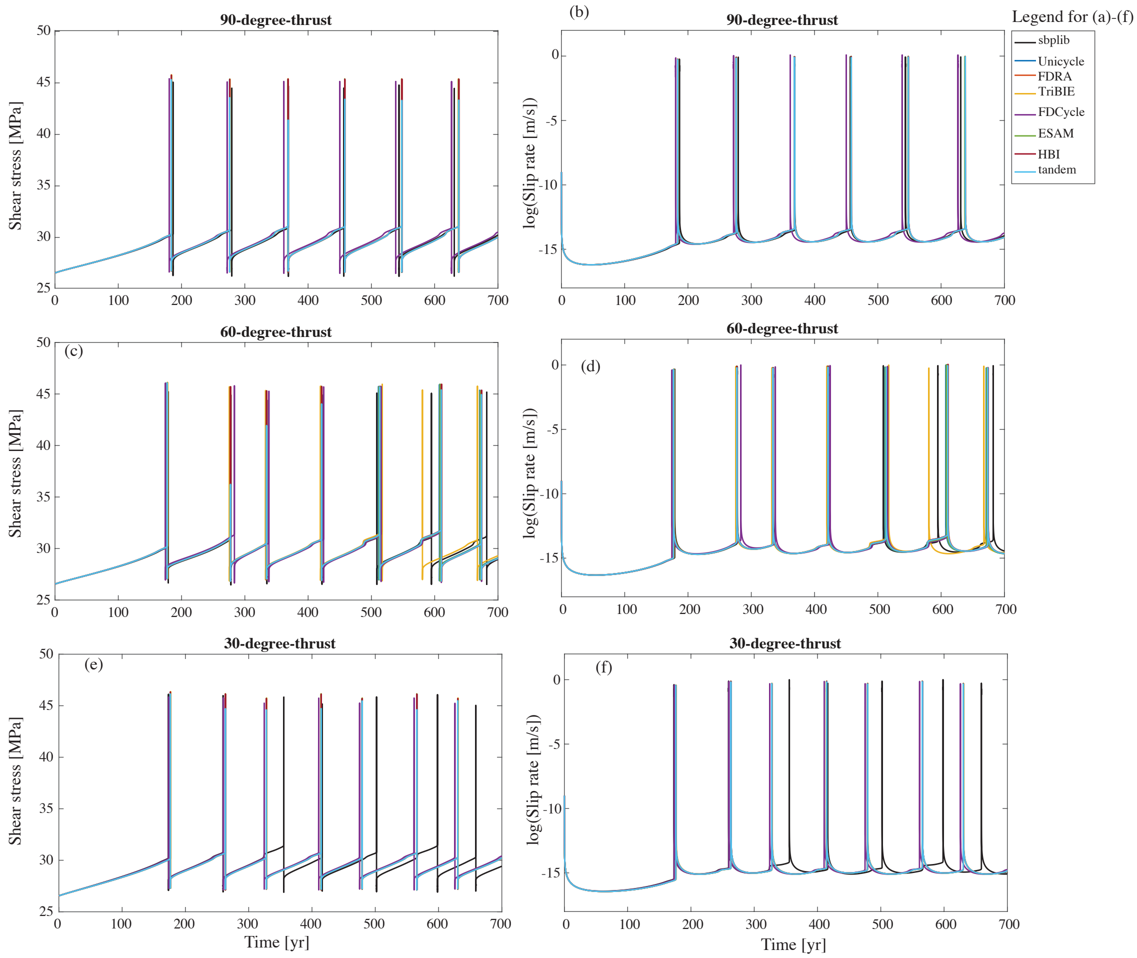

Figure 8: Long-term time-series of shear stress and slip rate for BP3-QD thrust faulting scenarios at $x_d = 7.5$ km for (a)-(b) 90°, (c)-(d) 60° and (e)-(f) 30°.

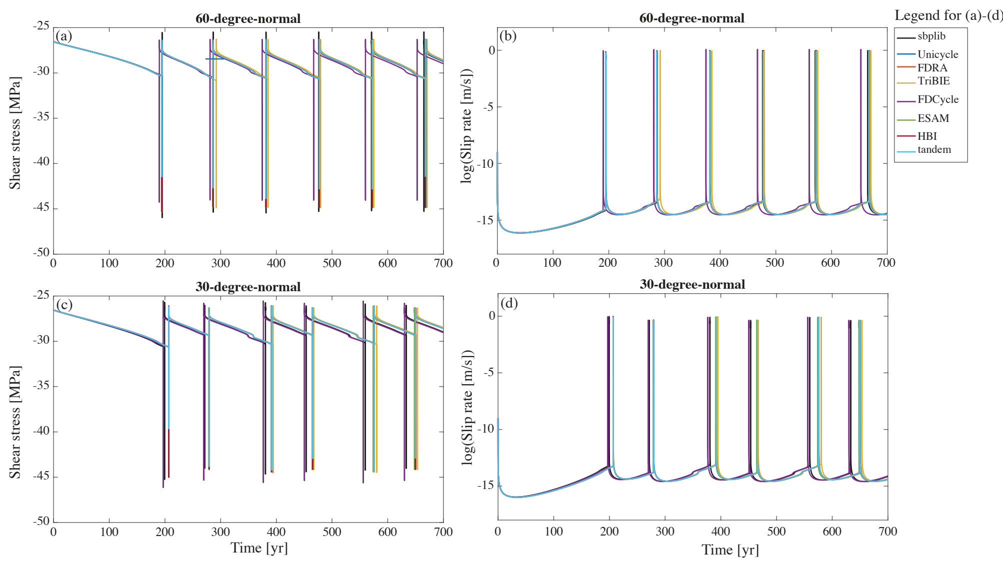

Figure 9: Long-term time-series of shear stress and slip rate for BP3-QD normal faulting scenarios at $x_d = 7.5$ km for (a)-(b) 60° and (c)-(d) 30°.

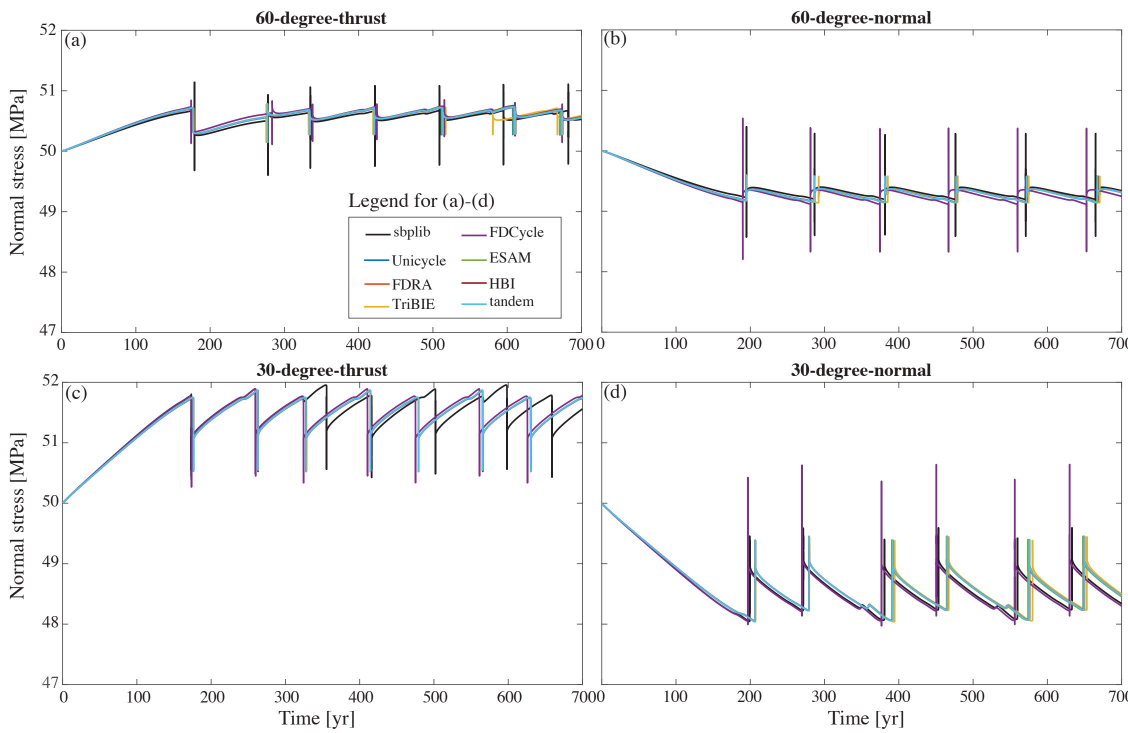

Figure 10: Long-term time-series of normal stress for BP3-QD thrust faulting scenarios at $x_d = 7.5$ km for (a)-(b) 60° thrust and normal faulting and (c)-(d) 30° thrust and normal faulting.

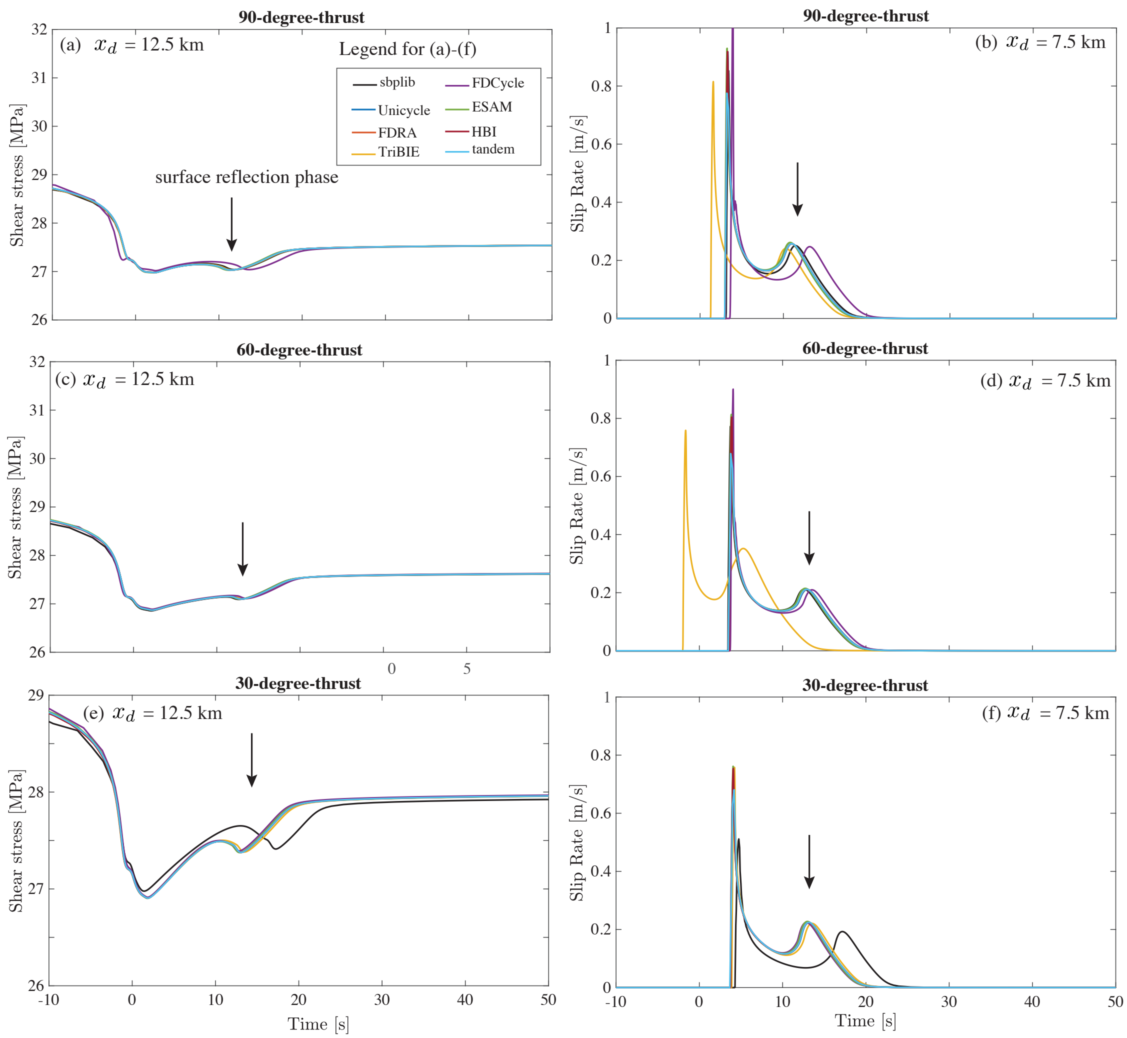

Figure 11: Coseismic behavior of BP3-QD models during the 8th event for thrust fault cases. Barring a few outliers, good agreements across codes exist for shear stresses at $x_d = 12.5$ km and slip rates at $x_d = 7.5$ km for (a)-(b) 90°, (c)-(d) 60°, and (e)-(f) 30°. Time (in seconds) is relative to the time at which the slip rate near the nucleation location ($x_d = 12.5$ km) first exceeds 10^{-1} m/s. The surface reflection phase is marked by a black arrow.

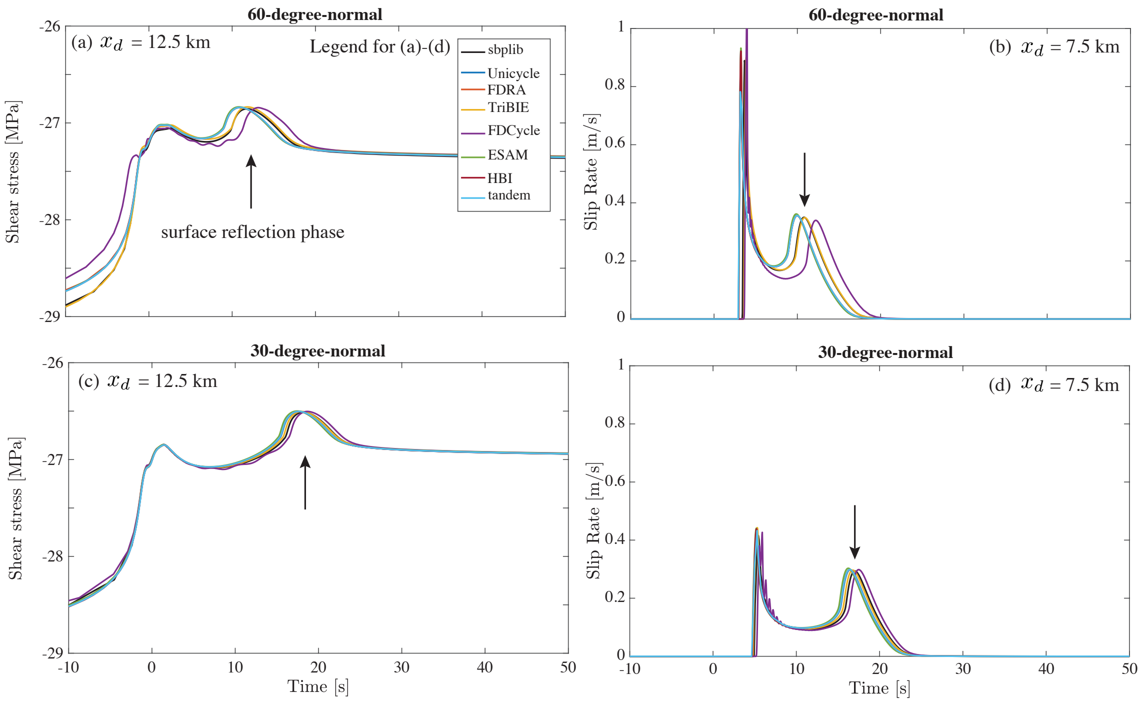

Figure 12: Coseismic behavior of BP3-QD models during the 8th event for normal fault cases. Good agreements across codes exist for shear stresses at $x_d = 12.5$ km and slip rates at $x_d = 7.5$ km for (a)-(b) 60°, and (e)-(f) 30°. Time (in seconds) is relative to the time at which the slip rate near the nucleation location ($x_d = 12.5$ km) first exceeds 10^{-1} m/s. The surface reflection phase is marked by a black arrow.

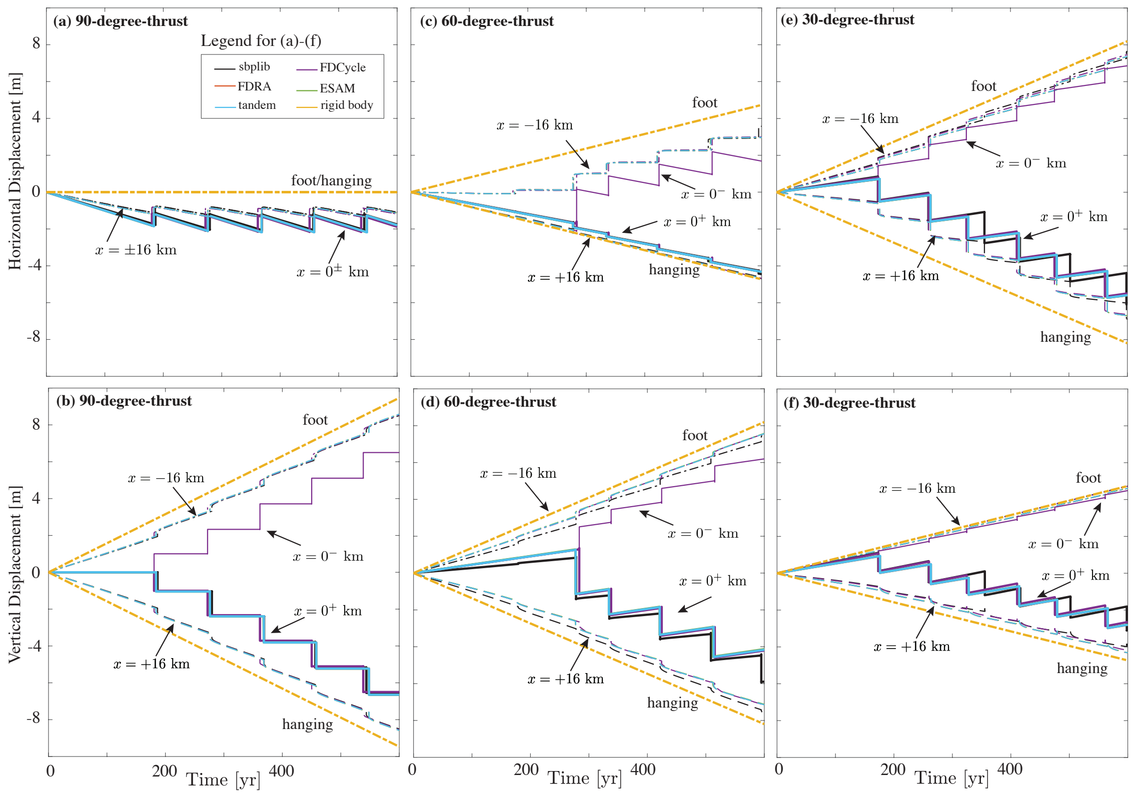

Figure 13: Horizontal and vertical components of surface displacement across a subset of codes at surface stations $x = 0^+, x = \pm 16$ km for thrust faulting cases with dip angles (a)-(b) 90°, (c)-(d) 60°, and (e)-(f) 30°. Also shown is surface station at $x = 0^-$ (not solicited by benchmark description) from FDCycle code for reference, and the rigid body (far field) translation (in yellow) where the text indicates motion on either the hanging or foot wall.

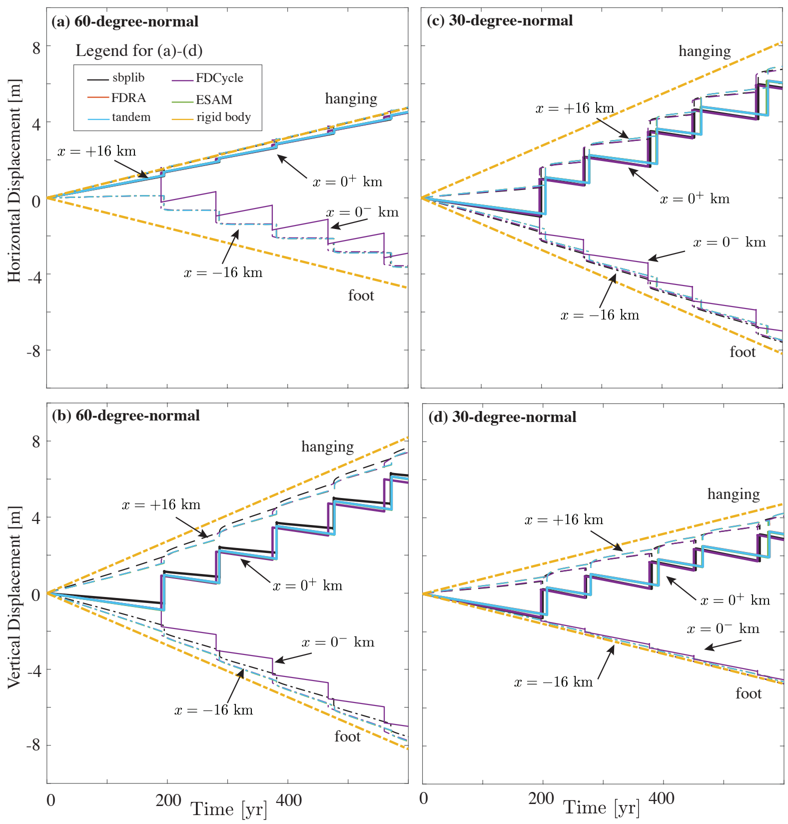

Figure 14: Horizontal and vertical components of surface displacement across a subset of codes at surface stations $x = 0^+, x = \pm 16$ km for normal faulting cases with dip angles (a)-(b) 60° and (c)-(d) 30°. Also shown is surface station at $x = 0^-$ (not solicited by benchmark description) from FDCycle code for reference, and the rigid body (far field) translation (in yellow) where the text indicates motion on either the hanging or foot wall.

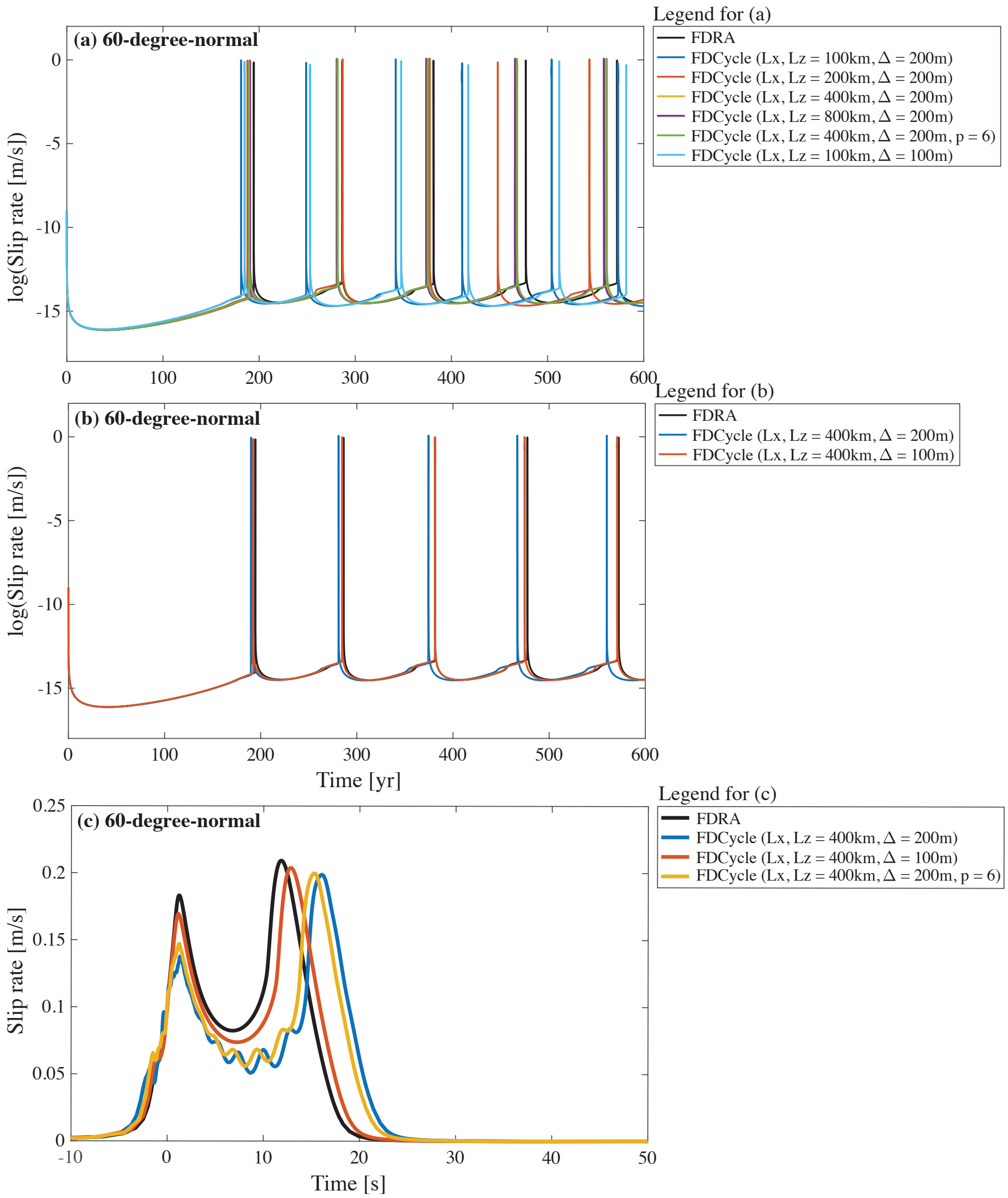

Figure 15: Results from the 60° normal faulting case from FDCycle compared to FDRA code (used as a reference). (a) Long-term time series of slip rate for results from FDCycle with varying domain sizes and different orders of accuracy and cell sizes. (b) Long-term times series results from a decreased cell size. (c) Better agreement in coseismic time series is achieved with larger domain sizes and smaller grid spacing, whereas increasing the order of accuracy provides only nominal improvement.